

A MATHEMATICAL PERSPECTIVE ON RADAR INTERFEROMETRY

MIKHAIL GILMAN* AND SEMYON TSYNKOV

Department of Mathematics, North Carolina State University
Campus Box 8205
Raleigh, NC 27695, USA

(Communicated by Margaret Cheney)

ABSTRACT. Radar interferometry is an advanced remote sensing technology that utilizes complex phases of two or more radar images of the same target taken at slightly different imaging conditions and/or different times. Its goal is to derive additional information about the target, such as elevation. While this kind of task requires centimeter-level accuracy, the interaction of radar signals with the target, as well as the lack of precision in antenna position and other disturbances, generate ambiguities in the image phase that are orders of magnitude larger than the effect of interest.

Yet the common exposition of radar interferometry in the literature often skips such topics. This may lead to unrealistic requirements for the accuracy of determining the parameters of imaging geometry, unachievable precision of image co-registration, etc. To address these deficiencies, in the current work we analyze the problem of interferometric height reconstruction and provide a careful and detailed account of all the assumptions and requirements to the imaging geometry and data processing needed for a successful extraction of height information from the radar data. We employ two most popular scattering models for radar targets: an isolated point scatterer and delta-correlated extended scatterer, and highlight the similarities and differences between them.

1. Introduction. The acronym RADAR stands for RADio Detection And Ranging. Nowadays, it is used as a plain word rather than acronym, because radar technology has become extremely widespread and common. The original radars were not designed as imaging instruments. Their imaging capacity has been introduced later. Very often it involves the synthesis of aperture, when the radar antenna mounted on an airplane or satellite emits a series of signals from different locations along the flight path (or orbit), and the image is obtained by processing the resulting series of returns, i.e., signals reflected off the target.

An image obtained by an Earth-observing synthetic aperture radar (SAR) approximately reconstructs the ground reflectivity. The latter is the capacity of the target to reflect the microwave signals emitted by the radar. The technique that combines two SAR images of the same scene and uses the phase difference between them to extract additional information is called interferometry. SAR interferometry (sometimes called InSAR) and polarimetric SAR interferometry (PolInSAR)

2020 *Mathematics Subject Classification.* Primary: 78A46, 78A48; Secondary: 78A55, 86A30.

Key words and phrases. Inverse scattering, synthetic aperture radar (SAR), interferogram, phase difference, height retrieval, imaging operator, point scatterer, extended scatterer, coherence.

* Corresponding author: Mikhail Gilman.

are rich in applications. In particular, these techniques help produce digital elevation maps and estimates of the aboveground biomass; they can reconstruct vertical structure of the vegetation layer and are also used for subsurface remote sensing, monitoring of glacier movement, change detection, and moving target identification [1, 34, 8, 24, 29, 27, 31, 25].

Mathematically, standard SAR images can be represented as convolution of the ground reflectivity function with the kernel that depends on the parameters of the imaging system and determines its key properties, such as resolution [11, 19, 6, 7]. However, extension of this convenient representation to interferometric imaging may be less than straightforward due to the specifics of the current exposition of SAR interferometry in the literature. First and foremost, the discussion of accuracy of the relevant parameters often appears vague, especially as it applies to system geometry. For example, given the image phase one can compute the elevation of the scatterer, but that may require knowing the coordinates of the antenna accurate to a fraction of the wavelength. In reality, however, the antenna location accuracy is orders of magnitude worse. Previous publications on extending the mathematical approach from plain SAR imaging to radar interferometry include [7, 39, 40]. In this work, we aim at addressing the issues that may still require attention.

Accordingly, the objective of the current paper is to provide a thorough account of radar interferometry via the convolution-based imaging operators developed for plain SAR. We restrict our analysis to the so-called cross-track interferometry, which is used primarily for building the elevation maps. In order to provide a detailed account of imaging geometry, we use the asymptotic analysis. We also formulate the accuracy requirements for the various parameters involved. For isolated point scatterers, we employ a deterministic framework, while for extended scatterers a stochastic framework is used under the assumption of a delta-correlated reflectivity. Finally, we analyze the technique of wavenumber adjustment (often called spectral range filtering) that helps improve the interferogram coherence. In doing so, we emphasize the differences between applying it to point scatterers and extended scatterers.

Section 2 provides a concise account of radar interferometry as traditionally presented in the literature. Section 3 introduces the framework of convolution-type imaging operators. Deficiencies of the traditional presentation of radar interferometry are summarized in Section 4. In Section 5, we analyze the interferometric imaging of isolated point scatterers using the operator framework of Section 3 and thus remedy the deficiencies identified in Section 4. In Section 6, we employ imaging operators for radar interferometry of extended scatterers and pay particular attention to the subject of interferometric coherence introduced in Section 6.1, as well as the wavenumber adjustment procedure. The problem of height retrieval for a vertically localized distributed scatterer is considered in Section 6.2. Section 6.3 compares the wavenumber adjustment procedure for extended scatterers against that for isolated point scatterers. Section 7 provides the concluding remarks. Finally, in the Appendix A we analyze the interferometric coherence in the Fourier space.

Note that plain SAR reconstructs the ground reflectivity as a function of two horizontal coordinates: range (normal to the antenna flight path and also referred to as cross-track) and azimuth (parallel to the flight path and known as along-track). The synthesis of aperture provides resolution in the azimuthal direction. At the same

time, radar interferometry is usually analyzed in the vertical cross-track plane. Although this ignores certain aspects of the InSAR signal processing, in particular, when the antenna beam is not orthogonal to the orbit [24, Section 2.5.5], we will be leaving the consideration of InSAR imaging in the full three-dimensional geometry outside the scope of this work. Specifically, this means that after the individual SAR images are obtained, the subsequent interferometric processing operates with image coordinates in the cross-track direction. Accordingly, we use the term “radar interferometry” rather than InSAR or PolInSAR whenever this does not lead to misunderstanding.

2. Traditional account of radar interferometry. A standard radar image is built by processing the interrogating signals emitted and received by the antenna after traveling to the target, getting reflected, and traveling back. Usually, the transmit and receive locations of the antenna coincide. Radar interferometry combines two radar images to extract additional information about the target. The most popular interferometric setup is the cross-track interferometry where a pair of images is acquired from two antenna locations that correspond to two slightly different incidence angles, see Fig. 1. Cross-track configurations can be realized using either a pair of antennas (single-pass interferometry) or a single antenna passing close to its original trajectory at a later time (repeat-pass interferometry). In this section, we present the main relations of the cross-track interferometry as can be found in the literature [1, 8, 24, 31, 16], except that we use our own system of notations that proves instrumental for the subsequent analysis.

Interferometry takes plain radar images as input. A procedure for obtaining those images is typically left out of discussion in the interferometric literature. For this reason, we postpone the description of this procedure until Section 3.

Let $\nu = \nu(\mathbf{z})$ be a complex-valued ground reflectivity function, where \mathbf{z} denotes spatial coordinates. Let the antenna be located at \mathbf{x} and let $R_{\mathbf{z}} = |\mathbf{z} - \mathbf{x}|$ be the distance between \mathbf{x} and \mathbf{z} . A key assumption needed for developing the interferometric framework is that for a given \mathbf{z} we can obtain the following quantity:

$$(1) \quad \angle \mathcal{I}(\mathbf{z}) = \angle \nu(\mathbf{z}) + 2 \cdot 2\pi R_{\mathbf{z}} / \lambda,$$

where λ is the signal wavelength and \angle denotes the argument of a complex number. The first term on the right-hand side of (1) is the complex argument, i.e., phase, of the ground reflectivity at \mathbf{z} , while the second term represents the accumulation of phase over the signal round-trip travel distance between the antenna and the target. We formally associate the expression on the right-hand side of (1) with the complex argument of the image, $\angle \mathcal{I}(\mathbf{z})$, even though the image $\mathcal{I}(\mathbf{z})$ itself is yet undefined (see Section 3 for its definition). For the rest of this section though, we will only need the complex argument $\angle \mathcal{I}(\mathbf{z})$.

Suppose that $\angle \mathcal{I}(\mathbf{z})$ can be obtained for two different antenna locations $\mathbf{x}^{(0)}$ and $\mathbf{x}^{(1)}$, called master and slave, that correspond to travel distances $R_{\mathbf{z}}^{(0)}$ and $R_{\mathbf{z}}^{(1)}$, respectively, see Fig. 1. Then, we can introduce the phase difference ψ_{01} as follows:

$$(2) \quad \psi_{01}(\mathbf{z}) \stackrel{\text{def}}{=} \angle \mathcal{I}^{(0)}(\mathbf{z}) - \angle \mathcal{I}^{(1)}(\mathbf{z}) = 2 \cdot 2\pi(R_{\mathbf{z}}^{(0)} - R_{\mathbf{z}}^{(1)}) / \lambda.$$

Clearly, $\psi_{01}(\mathbf{z})$ can be expressed as

$$\psi_{01}(\mathbf{z}) = \angle(\overline{\mathcal{I}^{(1)}(\mathbf{z})} \mathcal{I}^{(0)}(\mathbf{z})),$$

Solving this equation with respect to d and introducing

$$(5) \quad g = \frac{D}{R_z^{(0)}} \ll 1,$$

see (4), we have:

$$(6) \quad \begin{aligned} d &= R_z^{(0)} \left[1 - \sqrt{1 + g^2 - 2g \cos \beta(\mathbf{z})} \right] \\ &= R_z^{(0)} \left[1 - \left(1 + \frac{1}{2}g^2 - g \cos \beta(\mathbf{z}) - \frac{1}{2}g^2 \cos^2 \beta(\mathbf{z}) + \mathcal{O}(g^3) \right) \right] \\ &\approx R_z^{(0)} \left[g \cos \beta(\mathbf{z}) - \frac{1}{2}g^2 \sin^2 \beta(\mathbf{z}) \right]. \end{aligned}$$

The last line of (6) is obtained by dropping all the terms of order three and higher with respect to the small parameter $g = D/R_z^{(0)}$ defined in (5), and after the zeroth order terms have canceled. If we choose to drop the quadratic term as well, we arrive at the linearization:

$$(7) \quad R_z^{(0)} - R_z^{(1)} \approx D \cos \beta(\mathbf{z}).$$

Substituting (7) into (2), we obtain:

$$(8) \quad \psi_{01}(\mathbf{z}) = \frac{4\pi}{\lambda} D \cos \beta(\mathbf{z}).$$

Next, if H is the altitude of the master antenna, then the elevation of the point \mathbf{z} is

$$(9) \quad h(\mathbf{z}) = H - R_z^{(0)} \cos \theta(\mathbf{z}),$$

where $\theta(\mathbf{z})$ is the angle of incidence, i.e., the angle between $\mathbf{z} - \mathbf{x}^{(0)}$ and the negative vertical direction, see Fig. 1. If the positions of the two antennas are fixed, we have:

$$(10) \quad \theta(\mathbf{z}) + \beta(\mathbf{z}) = \text{const.}$$

Consider two particular cases. First, let the point \mathbf{z} be located above the ground level, and let the circle that passes through \mathbf{z} and is centered at $\mathbf{x}^{(0)}$ intersect the horizontal line $h = 0$ at a certain point \mathbf{T} so that $R_z^{(0)} = R_T^{(0)} = \text{const}$, see Fig. 1. From (8)–(10), we obtain:

$$(11) \quad \left. \frac{\partial \psi_{01}}{\partial h} \right|_{R_z^{(0)}=R_T^{(0)}} = - \left. \frac{d\psi_{01}}{d\beta} \frac{\partial \theta}{\partial h} \right|_{R_z^{(0)}=R_T^{(0)}} = \frac{4\pi}{\lambda} \left. \frac{D \sin \beta(\mathbf{z})}{R_T^{(0)} \sin \theta(\mathbf{z})} \right|_{R_z^{(0)}=R_T^{(0)}}.$$

Linearization of $\psi_{01}(\mathbf{z})$ around \mathbf{T} , combined with (11), yields:

$$(12) \quad (\psi_{01}(\mathbf{z}) - \psi_{01}(\mathbf{T})) \Big|_{R_z^{(0)}=R_T^{(0)}} \approx \frac{4\pi}{\lambda} \frac{D_{\perp}}{R_T^{(0)} \sin \theta(\mathbf{T})} h(\mathbf{z}) \Big|_{R_z^{(0)}=R_T^{(0)}},$$

where

$$D_{\perp} = D \sin \beta(\mathbf{T})$$

is often called the perpendicular baseline, see Fig. 1. Once the left-hand side of (12) is known, one can find the elevation $h(\mathbf{z})$ of the scatterer at point \mathbf{z} , see Fig. 1.

Another particular case corresponds to taking $h(\mathbf{z}') = h(\mathbf{T}) = 0$, as shown in Fig. 2. In this case, the distance $R_{z'}^{(0)}$ between $\mathbf{x}^{(0)}$ and \mathbf{z}' is no longer constant. To analyze the variation of the interferogram phase ψ_{01} with respect to the horizontal coordinate s , see Fig. 2, we differentiate the relation

$$H \tan \theta(\mathbf{z}') = \underbrace{R_T^{(0)} \sin \theta(\mathbf{T})}_{\text{const}} + s(\mathbf{z}')$$

In formula (16), $k = 2\pi/\lambda$, $k^{(1)} = 2\pi/\lambda_1$, and $\theta^{(1)}$ is the incidence angle for the slave antenna, see Fig. 2. Accordingly, formula (2) is modified as follows:

$$(17) \quad \begin{aligned} \tilde{\psi}_{01}(\mathbf{z}) &\stackrel{\text{def}}{=} \mathcal{L}\mathcal{I}^{(0)}(\mathbf{z}; k) - \mathcal{L}\mathcal{I}^{(1)}(\mathbf{z}; k_1) = 2 \cdot 2\pi \left(\frac{R_z^{(0)}}{\lambda} - \frac{R_z^{(1)}}{\lambda_1} \right) \\ &= 2(kR_z^{(0)} - k_1R_z^{(1)}). \end{aligned}$$

Introduce the interferometric angle $\Delta\theta = \theta(\mathbf{T}) - \theta^{(1)}(\mathbf{T})$. For $|\Delta\theta| \ll 1$, we can write: $\sin \theta^{(1)} \approx \sin \theta - \cos \theta \cdot \Delta\theta$. Hence, condition (16) is satisfied up to first order in $\Delta\theta$ if we take

$$(18) \quad k^{(1)} = k \left(1 + \frac{\Delta\theta}{\tan \theta(\mathbf{T})} \right).$$

From (18), we derive with the help of (2) and (17):

$$(19) \quad \tilde{\psi}_{01}(\mathbf{z}) = \psi_{01}(\mathbf{z}) - 2 \frac{\Delta\theta}{\tan \theta(\mathbf{T})} k R_z^{(1)}.$$

Then, formulae (11) and (13) are modified as follows:

$$(20) \quad \begin{aligned} \frac{\partial \tilde{\psi}_{01}}{\partial h} \Big|_{R_z^{(0)}=R_T^{(0)}} &= \frac{\partial \psi_{01}}{\partial h} \Big|_{R_z^{(0)}=R_T^{(0)}} - 2k \frac{\Delta\theta}{\tan \theta(\mathbf{T})} \frac{\partial R_z^{(1)}}{\partial h} \Big|_{R_z^{(0)}=R_T^{(0)}}, \\ \frac{\partial \tilde{\psi}_{01}}{\partial s} \Big|_{h(z')=h(\mathbf{T})} &= \frac{\partial \psi_{01}}{\partial s} \Big|_{h(z')=h(\mathbf{T})} - 2k \frac{\Delta\theta}{\tan \theta(\mathbf{T})} \frac{\partial R_{z'}}{\partial s} \Big|_{h(z')=h(\mathbf{T})}. \end{aligned}$$

To calculate the partial derivatives on the right-hand side of (20), we employ (9) and the law of cosines for the triangles $\Delta \mathbf{x}^{(0)} \mathbf{x}^{(1)} \mathbf{z}$ and $\Delta \mathbf{x}^{(0)} \mathbf{x}^{(1)} \mathbf{z}'$ (see Figs. 1 and 2):

$$(21) \quad \begin{aligned} \frac{\partial R_z^{(1)}}{\partial h} \Big|_{R_z^{(0)}=R_T^{(0)}} &= \frac{\partial R_z^{(1)}}{\partial \theta} \frac{\partial \theta}{\partial h} \Big|_{R_z^{(0)}=R_T^{(0)}} = - \frac{\partial \theta}{\partial h} \frac{\partial R_z^{(1)}}{\partial \beta} \Big|_{R_z^{(0)}=R_T^{(0)}} \\ &= - \frac{1}{R_z^{(0)} \sin \theta(\mathbf{z})} \frac{R_z^{(0)} D \sin \beta(\mathbf{z})}{R_z^{(1)}} \Big|_{R_z^{(0)}=R_T^{(0)}} \\ &= - \frac{D \sin \beta(\mathbf{z})}{R_z^{(1)} \sin \theta(\mathbf{z})} \Big|_{R_z^{(0)}=R_T^{(0)}}, \end{aligned}$$

$$(22) \quad \frac{\partial R_{z'}}{\partial s} \Big|_{h(z')=h(\mathbf{T})} = \frac{R_T^{(0)} \sin \theta(\mathbf{T}) - D \sin (\theta(\mathbf{T}) + \beta(\mathbf{T})) + s}{R_{z'}^{(1)}} \Big|_{h(z')=h(\mathbf{T})}.$$

Then, assuming that the displacements $|h|$ and $|s|$ are sufficiently small, e.g.,

$$\frac{|h|}{R_T^{(0)}} \sim \frac{|s|}{R_T^{(0)}} \lesssim |\Delta\theta| \ll 1,$$

we obtain from (20)–(22):

$$(23a) \quad \frac{\partial \tilde{\psi}_{01}}{\partial h} \Big|_{R_z^{(0)}=R_T^{(0)}} = \frac{\partial \psi_{01}}{\partial h} \Big|_{R_z^{(0)}=R_T^{(0)}} \cdot (1 + \mathcal{O}(\Delta\theta)),$$

$$(23b) \quad \frac{\partial \tilde{\psi}_{01}}{\partial s} \Big|_{h(z')=h(\mathbf{T})} = \frac{\partial \psi_{01}}{\partial s} \Big|_{h(z')=h(\mathbf{T})} \cdot \mathcal{O}(\Delta\theta).$$

This yields the following approximation:

$$(24) \quad \tilde{\psi}_{01}(\mathbf{z}) - \tilde{\psi}_{01}(\mathbf{T}) = \frac{4\pi}{\lambda} \frac{D_{\perp}}{R_{\mathbf{T}}^{(0)} \sin \theta(\mathbf{T})} h(\mathbf{z}) \cdot (1 + \mathcal{O}(\Delta\theta)).$$

Equation (24) is similar to (12). However, unlike in (12), the point \mathbf{z} in (24) is no longer restricted to the circle $R_{\mathbf{z}}^{(0)} = R_{\mathbf{T}}^{(0)}$. This is an implication of (23b). After dropping $\mathcal{O}(\Delta\theta)$, we can use (24) to calculate the elevation $h(\mathbf{z})$ from the difference of interferometric phases.

3. Mathematical treatment of radar imaging.

3.1. Formation of the image. Following [19, Chapter 2], we specify the radar interrogating signal as a narrow-band linear chirp (frequency modulated waveform) with the carrier frequency ω_0 , bandwidth B , duration τ , and rate $\alpha > 0$:

$$(25) \quad 2\alpha\tau = B \ll \omega_0 \quad \text{and} \quad B\tau \gg 1.$$

Using the notation χ_{τ} for the characteristic function of the interval $[-\tau/2, \tau/2]$:

$$(26) \quad \chi_{\tau}(t) = \begin{cases} 1, & t \in [-\tau/2, \tau/2], \\ 0, & \text{otherwise,} \end{cases}$$

we can write the expression for the chirp as follows:

$$(27) \quad P(t) = A(t)e^{-i\omega_0 t}, \quad \text{where} \quad A(t) = \chi_{\tau}(t)e^{-i\alpha t^2}.$$

We will associate the wavelength λ that appears in (1) with the central (or carrier) frequency of the chirp (27): $\lambda = 2\pi c/\omega_0$, where c is the speed of light (a constant). Note that the expression in (27) is complex-valued; for an interpretation, see Section 3.2 below.

Let the antenna be a point source located at \mathbf{x} (which may be either of the two locations, $\mathbf{x}^{(0)}$ or $\mathbf{x}^{(1)}$ in Fig. 1). The incident field u^i is the field emitted by the antenna that is excited by the pulse $P(t)$ of (27). u^i satisfies the constant-coefficient inhomogeneous wave equation:

$$(28) \quad \left(\frac{1}{c^2} \frac{\partial^2}{\partial t^2} - \Delta \right) u^i(t, \mathbf{z}) = \delta(\mathbf{z} - \mathbf{x})P(t).$$

Solution to equation (28) is given by the retarded potential:

$$(29) \quad u^i(t, \mathbf{z}) = \frac{1}{4\pi} \frac{P(t - |\mathbf{z} - \mathbf{x}|/c)}{|\mathbf{z} - \mathbf{x}|}.$$

Let $n = n(\mathbf{z})$ be the refractive index of the target material, which means that the propagation speed in the target region is $c/n(\mathbf{z})$. In vacuum, $n(\mathbf{z}) \equiv 1$. The overall field $u = u(t, \mathbf{z})$ satisfies the variable-coefficient wave equation (cf. equation (28)):

$$(30) \quad \left(\frac{n^2(\mathbf{z})}{c^2} \frac{\partial^2}{\partial t^2} - \Delta \right) u(t, \mathbf{z}) = \delta(\mathbf{z} - \mathbf{x})P(t).$$

It is convenient to represent u as the sum: $u = u^i + u^s$, where the term u^s is solely due to the deviation of the propagation speed from c in the target area (i.e., if there were no deviation: $n(\mathbf{z}) = 1$ everywhere, then we would have $u = u^i$ and

$u^s = 0$). The contribution $u^s = u^s(t, \mathbf{z})$ to the total field is called the scattered field. Subtracting equation (30) from (28), we get:

$$\left(\frac{1}{c^2} \frac{\partial^2}{\partial t^2} - \Delta\right) u^s(t, \mathbf{z}) = \frac{1 - n^2(\mathbf{z})}{c^2} \frac{\partial^2}{\partial t^2} (u^i + u^s).$$

The first Born approximation [19, Section 2.1.1] (also referred to as single scattering or weak scattering approximation) suggests that the term u^s on the right-hand side of this equation can be dropped, provided that the variation of the refractive index is small and the scattered field is also small compared to the incident field:

$$(31) \quad \left(\frac{1}{c^2} \frac{\partial^2}{\partial t^2} - \Delta\right) u^s(t, \mathbf{z}) = \frac{1 - n^2(\mathbf{z})}{c^2} \frac{\partial^2 u^i}{\partial t^2}.$$

Substituting (29) on the right-hand side of (31) and taking into account that the envelope $A(t)$ in (27) varies much slower than the fast carrier oscillation $e^{-i\omega_0 t}$, we obtain:

$$\left(\frac{1}{c^2} \frac{\partial^2}{\partial t^2} - \Delta\right) u^s(t, \mathbf{z}) \approx -\frac{1 - n^2(\mathbf{z})}{c^2} \frac{\omega_0^2}{4\pi} \frac{P(t - |\mathbf{z} - \mathbf{x}|/c)}{|\mathbf{z} - \mathbf{x}|}.$$

Then, the scattered field at the receiver $\mathbf{x}' \in \mathbb{R}^3$ is given by the Kirchhoff integral:

$$(32) \quad u^s(t, \mathbf{x}') \approx \int \nu(\mathbf{z}, \mathbf{x}, \mathbf{x}') P(t - |\mathbf{z} - \mathbf{x}|/c - |\mathbf{z} - \mathbf{x}'|/c) d\mathbf{z},$$

where

$$(33) \quad \nu(\mathbf{z}, \mathbf{x}, \mathbf{x}') = \frac{n^2(\mathbf{z}) - 1}{c^2} \frac{\omega_0^2}{16\pi^2 |\mathbf{z} - \mathbf{x}| |\mathbf{z} - \mathbf{x}'|}.$$

For typical imaging geometries, the emitting and receiving antennas \mathbf{x} and \mathbf{x}' are located at a large distance $\sim R$ from the target, where R is much larger than the characteristic size of the target area that determines the extent of variation of \mathbf{z} under the integral in (32). Consequently, the variation of the denominator in $\nu(\mathbf{z}, \mathbf{x}, \mathbf{x}')$ is small (see (33)), and since the numerator $n^2(\mathbf{z}) - 1$ is small in its own right (what enables the first Born approximation), we can replace $|\mathbf{z} - \mathbf{x}|$ and $|\mathbf{z} - \mathbf{x}'|$ in $\nu(\mathbf{z}, \mathbf{x}, \mathbf{x}')$ with the same constant quantity R . We can also assume that the emitting and receiving locations coincide, which is common. Then,

$$(34) \quad u^s(t, \mathbf{x}) \approx \int \underbrace{\frac{n^2(\mathbf{z}) - 1}{c^2} \frac{\omega_0^2}{16\pi^2 R^2}}_{\nu(\mathbf{z})} P(t - 2 \underbrace{|\mathbf{z} - \mathbf{x}|/c}_{R_z}) d\mathbf{z}.$$

The function $\nu(\mathbf{z})$ under the integral in (34) is called the ground reflectivity function.

The goal of radar imaging is to reconstruct the reflectivity function $\nu(\mathbf{z})$ given the scattered field $u^s(t, \mathbf{x})$, i.e., invert (34) and obtain $\nu(\mathbf{z})$ while interpreting $u^s(t, \mathbf{x})$ as the data. The inversion is rendered by application of a matched filter to the received signal. The matched filter P_{filt} is a complex conjugate of the antenna signal (27):

$$(35) \quad P_{\text{filt}}(t, \mathbf{y}) = \overline{P(t - t_y)} = \chi_\tau(t - t_y) e^{i\omega_0(t - t_y) + i\alpha(t - t_y)^2},$$

where

$$(36) \quad t_y = \frac{2|\mathbf{x} - \mathbf{y}|}{c} = \frac{2R_y}{c}.$$

Accordingly, the image is expressed as

$$(37) \quad I(\mathbf{y}) = \int P_{\text{filt}}(t, \mathbf{y}) u^s(t, \mathbf{x}) dt = \int \overline{P\left(t - \frac{2R_y}{c}\right)} u^s(t, \mathbf{x}) dt.$$

The function $I(\mathbf{y})$ approximates $\nu(\mathbf{z})$ of (34), see Section 3.3. The spatial argument \mathbf{y} is often referred to as focusing location (or focusing parameter). The difference in notations between $I(\mathbf{y})$ of (37) and $\mathcal{I}(\mathbf{z})$ of Section 2 is intentional, see Sections 3.3 and 5.1.

Substituting (34) into (37), we obtain the integral imaging operator:

$$(38) \quad I(\mathbf{y}) = \int W(\mathbf{y}, \mathbf{z}) \nu(\mathbf{z}) d\mathbf{z}.$$

Its kernel W (also called the point spread function, or PSF) is given by

$$(39) \quad W(\mathbf{y}, \mathbf{z}) = \int \overline{P\left(t - \frac{2R_{\mathbf{y}}}{c}\right)} P\left(t - \frac{2R_{\mathbf{z}}}{c}\right) dt.$$

It can be shown (see [19, Section 2.6]) that W depends only on the difference of its two arguments \mathbf{y} and \mathbf{z} (via the difference of the distances $R_{\mathbf{y}}$ and $R_{\mathbf{z}}$):

$$W(\mathbf{y}, \mathbf{z}) \equiv W(\mathbf{y} - \mathbf{z}) \equiv W(R_{\mathbf{y}} - R_{\mathbf{z}}).$$

Hence, formula (38) reduces to a convolution:

$$(40) \quad I(\mathbf{y}) = \int W(\mathbf{y} - \mathbf{z}) \nu(\mathbf{z}) d\mathbf{z} = [W * \nu](\mathbf{y}).$$

Substituting (25)–(27) into (39), we express the PSF W as a function of one scalar argument:

$$(41) \quad W(l) = e^{-2i\omega_0 l/c} \cdot V(l) = e^{-2i\omega_0 l/c} \cdot \tau \operatorname{sinc}\left(\frac{Bl}{c}\right),$$

where $l = R_{\mathbf{y}} - R_{\mathbf{z}}$ and $\operatorname{sinc} x = \frac{\sin x}{x}$ is the spherical Bessel function of order 0. The central portion of the $\operatorname{sinc}(\cdot)$ in (41) between its first negative and first positive zero: $\frac{Bl}{c} = \pm\pi$, is referred to as its main lobe; the portions of the $\operatorname{sinc}(\cdot)$ between its subsequent zeros to the left and right from the origin are called the sidelobes.

3.2. Complex-valued signal and image. Most of the functions introduced in Section 3.1, including the emitted signal $P(t)$ in (27), scattered field $u^s(t, \mathbf{x}')$ in (32), and image $I(\mathbf{y})$ in (37), are complex-valued. The motivation for using the complex form can be seen, e.g., in the convenience of expressing the phase of $P(t)$ as $\angle P(t) = -\chi_r(t) \cdot (\omega_0 t + \alpha t^2)$. Yet these functions represent, or are proportional to, certain physical values, such as the electric field intensity or antenna voltage, that are intrinsically real-valued. The procedure of converting the band-limited real-valued data (e.g., the real part of $P(t)$ given by (27)) to the complex form along with stripping the carrier frequency is called the quadrature demodulation, see [10, Section 4B.1] or [27, Section 1.3]. In essence, the real and imaginary part of the demodulated function are obtained by multiplying the original real-valued signal by two copies of the carrier sinusoid with a shift of $\pi/2$ between them, followed by integration. Throughout this work, we assume that this procedure stands behind all complex-valued functions, possibly with the subsequent restoration of the high-frequency term, such as $e^{-i\omega_0 t}$ or e^{2ikl} . In addition, we note that the reference values of permittivity of real-world materials are often complex-valued, which represents the phase shift at reflection and refraction. This justifies the use of complex-valued functions on both sides of (32), including the cases where the first Born approximation formula (33) for ν is not valid.

3.3. Convergence. To analyze in what sense the image I approximates the reflectivity ν , we consider a simplified one-dimensional version of (40) (recall, $k = \frac{\omega_0}{c}$):

$$(42) \quad I_B(y) = \int W_B(y - z) \cdot \nu(z) dz = \tau \int \text{sinc}\left(\frac{B(y - z)}{c}\right) e^{-2ik(y-z)} \nu(z) dz,$$

where the subscript “ B ” indicates that the imaging kernel (PSF) corresponds to the specific value of the chirp bandwidth B , see formula (25).

Proposition 1. *For a fixed chirp rate, $\alpha = \text{const}$, the image $I_B(y)$ given by (42) converges weakly as $B \rightarrow \infty$ to a constant multiple of the reflectivity function $\nu(y)$.*

Proof. Following [20] and [19, Section 7.2], we first modify the image I_B by multiplying both sides of equation (42) with the exponential factor e^{2iky} :

$$\mathcal{I}_B(y) \equiv I_B(y)e^{2iky} = \tau \int \text{sinc}\left(\frac{B(y - z)}{c}\right) e^{2ikz} \nu(z) dz.$$

Next, let $\varphi(y)$ be a Schwartz test function. Then,

$$(43) \quad \begin{aligned} \int_{-\infty}^{\infty} \mathcal{I}_B(y)\varphi(y)dy &= \int \tau \int \text{sinc}\left(\frac{B(y - z)}{c}\right) e^{2ikz} \nu(z) dz \varphi(y) dy \\ &= \int \tau \int \text{sinc}\left(\frac{B(y - z)}{c}\right) \varphi(y) dy e^{2ikz} \nu(z) dz. \end{aligned}$$

The dy (i.e., interior) integral on the second line of (43) is the Fourier transform in y of the product $\text{sinc}\left(\frac{B(y-z)}{c}\right)\varphi(y)$ taken at the (spatial) frequency $\kappa = 0$. Consequently,

$$(44) \quad \tau \int \text{sinc}\left(\frac{B(y - z)}{c}\right) \varphi(y) dy = \tau \frac{\pi c}{B} [e^{-i\kappa z} \chi_{\frac{2B}{c}} * \hat{\varphi}](\kappa) \Big|_{\kappa=0},$$

because

$$\int_{-\infty}^{\infty} \text{sinc}\left(\frac{B(y - z)}{c}\right) e^{-i\kappa y} dy = \frac{\pi c}{B} e^{-i\kappa z} \chi_{\frac{2B}{c}}(\kappa).$$

On the right-hand side of the previous equation, $\chi_{\frac{2B}{c}}(\cdot)$ is the characteristic function defined in (26). Also in (44): $\hat{\varphi}(\kappa) = \int_{-\infty}^{\infty} \varphi(y) e^{-i\kappa y} dy$. Since $\tau = \frac{B}{2\alpha}$ (see formula (25)), we obtain:

$$(45) \quad \begin{aligned} \tau \int \text{sinc}\left(\frac{B(y - z)}{c}\right) \varphi(y) dy &= \frac{\pi c}{2\alpha} \int_{-\infty}^{\infty} \hat{\varphi}(\xi) \chi_{\frac{2B}{c}}(\kappa - \xi) e^{-i(\kappa - \xi)z} d\xi \Big|_{\kappa=0} \\ &= \frac{\pi c}{2\alpha} \int_{-\infty}^{\infty} \hat{\varphi}(\xi) \chi_{\frac{2B}{c}}(\xi) e^{i\xi z} d\xi = \frac{\pi c}{2\alpha} \int_{-\frac{B}{c}}^{\frac{B}{c}} \hat{\varphi}(\xi) e^{i\xi z} d\xi \\ &= \frac{\pi^2 c}{\alpha} \frac{1}{2\pi} \int_{-\frac{B}{c}}^{\frac{B}{c}} \hat{\varphi}(\xi) e^{i\xi z} d\xi \rightarrow \frac{\pi^2 c}{\alpha} \varphi(z), \text{ as } B \rightarrow \infty, \end{aligned}$$

where we took into account that $\chi_{\frac{2B}{c}}(\cdot)$ is an even function. The last line in (45) implies that $\tau \text{sinc}\left(\frac{B(y-z)}{c}\right)$ converges weakly to $\frac{\pi^2 c}{\alpha} \delta(y - z)$ as the bandwidth B of the chirp increases.

Therefore, substituting (45) into (43) we have:

$$(46) \quad \int_{-\infty}^{\infty} \mathcal{I}_B(y)\varphi(y)dy \rightarrow \frac{\pi^2 c}{\alpha} \int e^{2ikz} \nu(z) \varphi(z) dz, \text{ as } B \rightarrow \infty.$$

Equation (46) means that $\mathcal{I}_B(y) \rightarrow \text{const} \cdot \nu(y)e^{2iky}$ as $B \rightarrow \infty$ in the sense of distributions. As $\mathcal{I}_B(y) = I_B(y)e^{2iky}$, we conclude that $I_B(y) \rightarrow \text{const} \cdot \nu(y)$ as $B \rightarrow \infty$. \square

3.4. Point scatterer. In reality, the bandwidth B cannot become arbitrarily large. On the contrary, most imaging radars are narrow-band, and their bandwidth is a small fraction of the carrier frequency so that $B/\omega_0 \ll 1$ (see formula (25)). Therefore, the result of Proposition 1 never fully applies in practice, and the image remains an “under-converged” approximation of the original reflectivity. The specific form of ν that allows one to see most intuitively the difference between the original reflectivity and its image is that of an isolated point scatterer.

The point scatterer is introduced formally, taking advantage of the fact that the convergence established by Proposition 1 holds for a broader class of functions ν , Schwartz distributions, than those for which the first Born approximation of Section 3.1 is valid.

Let us first change the integration variable in formula (34) for convenience:

$$u^s(t, \mathbf{x}) = \int \nu(\tilde{\mathbf{z}})P(t - 2R_{\tilde{\mathbf{z}}}/c)d\tilde{\mathbf{z}}.$$

Then, the point scatterer at a given fixed location \mathbf{z} is defined as

$$(47) \quad \nu(\tilde{\mathbf{z}}) = \nu_0\delta(\tilde{\mathbf{z}} - \mathbf{z}).$$

This yields the scattered field:

$$(48) \quad u^s(t, \mathbf{x}) = \nu_0P(t - 2R_{\mathbf{z}}/c)$$

and the image:

$$(49) \quad I(\mathbf{y}) = \nu_0 \cdot \tau e^{-2i\omega_0(R_{\mathbf{y}} - R_{\mathbf{z}})/c} \text{sinc}\left(B \frac{R_{\mathbf{y}} - R_{\mathbf{z}}}{c}\right).$$

In the vertical cross-track plane (see Fig. 1), the main lobe of the sinc in (49) specifies an annulus of central radius $R_{\mathbf{z}}$ and thickness $2\Delta_{\text{R}}$ (see Fig. 3), where

$$(50) \quad \Delta_{\text{R}} = \frac{\pi c}{B}.$$

The absolute value $|I(\mathbf{y})|$ of the image (49) as a function of $R_{\mathbf{y}} - R_{\mathbf{z}}$ has a global maximum at $R_{\mathbf{y}} - R_{\mathbf{z}} = 0$. The distance from this maximum to the first zero of the sinc is precisely Δ_{R} of (50). It is commonly accepted that two point scatterers located further away than Δ_{R} from one another can be told apart on the image, while those closer than Δ_{R} cannot because their respective maxima may appear indistinguishable. Therefore, the quantity Δ_{R} of (50) is referred to as resolution (range resolution in full-fledged SAR, see [19, Section 2.6]).

The notion of resolution implies that not only $\mathbf{y} = \mathbf{z}$, but any other point within the ring-shaped shaded area in Fig. 3:

$$(51) \quad |R_{\mathbf{y}} - R_{\mathbf{z}}| < \Delta_{\text{R}} \quad \Leftrightarrow \quad B \frac{|R_{\mathbf{y}} - R_{\mathbf{z}}|}{c} < \pi,$$

for example, $\mathbf{y} = \mathbf{z}'$ or $\mathbf{y} = \mathbf{z}''$ (see Fig. 3), can be associated with the point scatterer of type (47) that yields the image $I(\mathbf{y})$ of (49). With no information on elevation, all such points remain indistinguishable. Knowledge of elevation h reduces the ambiguity and restricts the possible location of the scatterer to a horizontal line

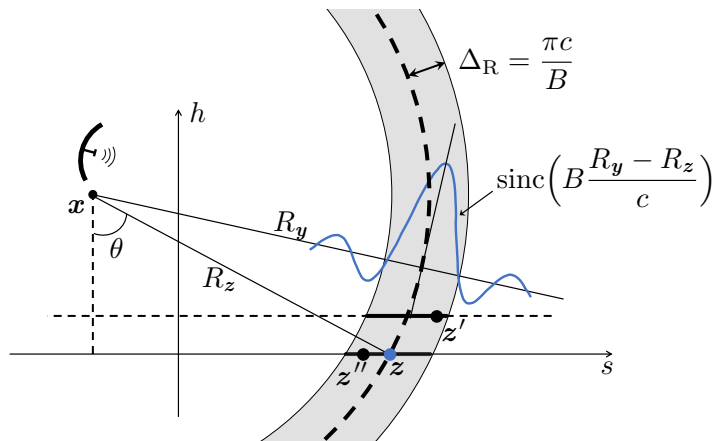


FIGURE 3. The annulus in the vertical cross-track plane due to the main lobe of the sinc in (49). It is centered at \boldsymbol{x} and has central radius R_z . Its thickness $2\Delta_R$ is defined by the system bandwidth B , see formula (50). Vertical localization of radar targets can be performed using either interferometry or external information about the elevation.

segment of length $\sim 2\Delta_R$.¹ The elevation h can be inferred from interferometry or otherwise from some external considerations, e.g., that all scatterers lie on the horizontal line $h = 0$.

The ambiguity in the location of the scatterer implies that one cannot accurately recover the complex argument of the reflectivity from formula (49). Indeed, as $B \ll \omega_0$ (see (25)), the phase of the image (49) makes many revolutions in-between $\pm\Delta_R$:

$$(52) \quad \frac{\Delta_R}{\lambda} = 2 \frac{\omega_0}{B} \gg 1.$$

In the one-dimensional setting of Section 3.3, the image of a point scatterer obtained by the radar system with bandwidth B is (cf. formula (49))

$$I_B(y) = \nu_0 W_B(y - z) = \nu_0 \tau \operatorname{sinc}\left(\frac{B(y - z)}{c}\right) e^{-2ik(y - z)}.$$

According to Proposition 1, $I_B(y) \rightarrow \text{const} \cdot \nu_0 \delta(y - z)$ weakly as $B \rightarrow \infty$. In simple words, for larger B the central lobe of the $\operatorname{sinc}(\cdot)$ becomes narrower and taller and “approaches” the Dirac δ -function (see the discussion right after equation (45)).

4. Deficiencies of the traditional account of interferometry. The traditional treatment of radar interferometry (Section 2) has enabled many successful applications (Section 1). Yet no thorough mathematical analysis of this subject is available in the literature. Extension of the approach of Section 3 along the lines of Section 2 may be hampered by the lack of rigor in deriving formulae (12), (14), (24) or their equivalents. That may lead to an ambiguous interpretation of the various terms in interferometric relations and unrealistic requirements for the imaging system.

¹Geometrically, there will be two segments that are symmetrical about the vertical axis passing through the antenna location, but one of them is eliminated by knowing the direction of the antenna beam (e.g., it can be the positive direction of the s -axis in Fig. 3).

1. **Image co-registration.** The values of $\mathcal{I}^{(1)}(\mathbf{z})$ and $\mathcal{I}^{(0)}(\mathbf{z})$ in the interferogram (3) must correspond to the same spatial location \mathbf{z} . However, these two images are taken by different devices and/or at different times. Thus, they must be co-registered first. As the actual images are functions of \mathbf{y} , see (40), the co-registration must be performed w.r.t. \mathbf{y} . The best achievable accuracy of the existing co-registration techniques is a few percent of the resolution size [36, 35, 23, 15]. Therefore, if a certain image feature corresponds to $\mathbf{y}^{(0)}$ on the master image and $\mathbf{y}^{(1)}$ on the slave, we may have:

$$(53) \quad |\mathbf{y}^{(0)} - \mathbf{y}^{(1)}| \gtrsim 10^{-2} \Delta_{\mathbf{R}}.$$

As the typical relative bandwidth B/ω_0 is also about a few percent [32], formulae (49), (52), and (53) indicate that misregistration can introduce phase errors greater than π .

2. **Antenna location.** The travel distances $R_z^{(0)}$ and $R_z^{(1)}$ in equation (2) depend on the coordinates of the antenna, and subsequent geometric calculations based on (2) involve those coordinates. Yet the errors in determining the location of the antenna are typically much larger than the wavelength. Although laser systems can yield a centimeter-scale accuracy in orbital measurements, the accuracy of the routinely provided trajectory data is on the order of one meter or worse [41, 13, 38]. Given a typical radar wavelength between a few centimeters and a meter, such accuracy is insufficient to calculate the propagation phase accurate to a small fraction of π .
3. **Linearization of distances.** Formula (7) is a linear approximation of the true expression for $R_z^{(0)} - R_z^{(1)}$, which is given by the first line of (6). From the third line of (6), we see that the neglected terms are about $g^2 = \frac{D^2}{2R_z^{(0)}}$. With $D \sim 1km$ and $R_z^{(0)} \sim 10^3 km$, this evaluates to about $0.5m$. For an X-band radar with the wavelength $\sim 3cm$, this accuracy is insufficient, as it will lead to errors $> \pi$ in equation (8). A justification of why the terms $\sim \frac{D^2}{R_z^{(0)}}$ in (6) can be disregarded is usually missing in the literature.
4. **Missing data for height reconstruction.** Consider equation (12) that yields the scatterer elevation h . The difference of interferometric phases on its left-hand side provides the data. However, this left-hand side may vanish if the points \mathbf{z} and \mathbf{T} are sufficiently close to one another in the sense of (51). In that case, they may correspond to the same focusing location, i.e., appear indistinguishable:

$$(54) \quad \begin{aligned} I^{(0)}(\mathbf{z}) &= I^{(0)}(\mathbf{T}) = I^{(0)}(\mathbf{y}^{(0)}), \\ I^{(1)}(\mathbf{z}) &= I^{(1)}(\mathbf{T}) = I^{(1)}(\mathbf{y}^{(1)}). \end{aligned}$$

Then,

$$(55) \quad (\psi_{01}(\mathbf{z}) - \psi_{01}(\mathbf{T})) \Big|_{R_z^{(0)}=R_T^{(0)}} = \angle[\overline{I^{(1)}(\mathbf{z})} I^{(0)}(\mathbf{z})] - \angle[\overline{I^{(1)}(\mathbf{T})} I^{(0)}(\mathbf{T})] \equiv 0.$$

A necessary condition for the first line of (54) to hold is $|R_z^{(0)} - R_T^{(0)}| < \Delta_{\mathbf{R}}$; it is always satisfied because for the master image $R_z^{(0)} = R_T^{(0)}$ (see Fig. 1). A necessary condition for the second line of (54) to hold is $|R_z^{(1)} - R_T^{(1)}| < \Delta_{\mathbf{R}}$. Using (21), we see that it is true as long as $h(\mathbf{z}) \lesssim \Delta_{\mathbf{R}}(\Delta\theta)^{-1}$, because $\Delta\theta \approx \frac{D}{R_T^{(0)}}$. For common configurations, $\Delta_{\mathbf{R}}(\Delta\theta)^{-1}$ evaluates to about several

kilometers. The elevations lower than that may appear indiscernible because the left-hand side of (12) will be equal to zero, see (55).

5. **Reference location and master/slave asymmetry.** The elevation h obtained via (12) or (24) is elevation above the reference point \mathbf{T} (see Fig. 1). The latter, in turn, is defined with respect to the master antenna at $\mathbf{x}^{(0)}$ ($\mathbf{x}^{(0)}$ is at altitude H above \mathbf{T}). The effect of swapping the master and slave antenna between $\mathbf{x}^{(0)}$ and $\mathbf{x}^{(1)}$ should be investigated. Predicting the magnitude of this effect for formula (17) is not trivial.
6. **Flat Earth phase removal.** Two approaches have been introduced in Section 2 for the flat Earth phase removal. The first method, which is based on formulae (14), (15), is straightforward. The second one is given by (16)–(24); it reveals some limitations if considered for an interferometric pair produced by identical radar systems. In particular, the frequency adjustment of real systems is usually limited by the available bandwidth, and via (18), this translates into an upper limit on the interferometric angle: $|\Delta\theta| \leq \tan\theta \cdot B/\omega_0$. No physical interpretation of this effect has been proposed; in particular, it is not clear whether the target properties play any role.

The analysis of interferometric radar imaging in Section 5 addresses the deficiencies outlined in items 1 through 5. It builds upon the mathematical framework for radar imaging developed in Section 3 and does not involve any unrealistic assumptions. We treat both antennas in the same fashion and thoroughly analyze the approximation accuracy in geometric calculations. Item 6 is addressed in Section 6. In particular, we show that the procedure of wavenumber adjustment described by (16)–(24) is most helpful when dealing with extended scatterers, whereas for isolated point scatterers, the standard approach to flat Earth phase removal based on (14), (15) is more relevant.

5. **Radar interferometry for point scatterers.**

5.1. **Radar image and interferometric phase.** Similarly to Section 3.3, let us redefine the image $I(\mathbf{y})$ given by (40) as follows:

$$(56) \quad \mathcal{I}(\mathbf{y}) = I(\mathbf{y})e^{2i\omega_0 R_y/c}.$$

On the right-hand side of (56), the original image $I(\mathbf{y})$ is merely multiplied with a known function of \mathbf{y} . In particular, the image of a point scatterer (49) becomes:

$$(57) \quad \mathcal{I}(\mathbf{y}) = \nu_0 \cdot \tau e^{2i\omega_0 R_z/c} \operatorname{sinc}\left(B \frac{R_y - R_z}{c}\right).$$

Expression (57) was used in [1]. For the complex phase of (57) we have ($\lambda = \frac{2\pi c}{\omega_0}$):

$$(58) \quad \angle \mathcal{I}(\mathbf{y}) = \angle \nu_0 + 2 \cdot 2\pi R_z/\lambda.$$

The right-hand sides of equations (58) and (1) coincide. Therefore, the entire right-hand side of (1) can be obtained by evaluating the complex argument of $\mathcal{I}(\mathbf{y})$. Moreover, as the right-hand side of (58) does not depend on \mathbf{y} , it can be evaluated for any \mathbf{y} on the left-hand side. As such, no precise co-registration of the images $\mathcal{I}^{(0)}(\mathbf{y})$ and $\mathcal{I}^{(1)}(\mathbf{y})$ is required. This addresses item 1 in Section 4. Indeed, even if a certain feature \mathbf{z} corresponds to different $\mathbf{y}^{(0)}$ and $\mathbf{y}^{(1)}$ on the two images, we still have according to (58) (cf. formulae (2), (3)):

$$(59) \quad \angle q(\mathbf{z}) = \angle [\overline{\mathcal{I}^{(1)}(\mathbf{y}^{(1)})} \mathcal{I}^{(0)}(\mathbf{y}^{(0)})] = 2 \cdot 2\pi(R_z^{(0)} - R_z^{(1)})/\lambda.$$

The role of co-registration is further discussed in Section 6.1 and Appendix A.

Of course, for the previous conclusions to hold, the contribution from any other scatterers to $\mathcal{I}(\mathbf{y})$ should be negligible. For example, suppose that there are two point scatterers located at \mathbf{T} and \mathbf{z}' (see Fig. 2):

$$(60) \quad \nu(\mathbf{z}) = \nu_{\mathbf{T}}\delta(\mathbf{z}) + \nu'_0\delta(\mathbf{z} - \mathbf{z}').$$

Let $\mathbf{y}_{\mathbf{T}}^{(0)}$ and $\mathbf{y}'^{(0)}$ satisfy (51) for the master antenna:

$$|R_{\mathbf{y}_{\mathbf{T}}}^{(0)} - R_{\mathbf{T}}^{(0)}| \ll \Delta_{\mathbf{R}}, \quad |R_{\mathbf{y}'}^{(0)} - R_{\mathbf{z}'}^{(0)}| \ll \Delta_{\mathbf{R}}.$$

To use formula (14) for the target (60), we must have similarly to (58):

$$(61) \quad \angle \mathcal{I}^{(0)}(\mathbf{y}_{\mathbf{T}}^{(0)}) \approx \angle \nu_{\mathbf{T}} + 2 \cdot 2\pi R_{\mathbf{T}}^{(0)} / \lambda, \quad \angle \mathcal{I}^{(0)}(\mathbf{y}'^{(0)}) \approx \angle \nu'_0 + 2 \cdot 2\pi R_{\mathbf{z}'}^{(0)} / \lambda.$$

If the two scatterers are sufficiently far from each other:

$$(62) \quad |R_{\mathbf{z}'}^{(0)} - R_{\mathbf{T}}^{(0)}| \gg \Delta_{\mathbf{R}},$$

then one may expect that relations (61) will hold because the ‘‘cross-contamination,’’ i.e., influence of $\nu_{\mathbf{T}}$ and ν'_0 on $\mathcal{I}^{(0)}(\mathbf{y}'^{(0)})$ and $\mathcal{I}^{(0)}(\mathbf{y}_{\mathbf{T}})$, respectively, will be small due to attenuation by the sinc function in (57). The same is true for the slave antenna.

5.2. Interferogram phase in slant coordinates. We will replace the analysis of Section 2 with a symmetric and more consistent derivation that employs the slanted frame of reference shown in Fig. 4. The slant and cross-slant coordinates are denoted by u and v , respectively, so that, e.g., $\mathbf{z} = (z_u, z_v)$. The angle between the negative u -axis and vertical direction is $\theta = \text{const}$. A reference point $\mathbf{T} = (0, 0)$ is specified in the target area. Instead of the master and slave antennas (see Fig. 1), we consider two coequal antennas in the vicinity of $\mathbf{R} \equiv (-R, 0)$, where $R = \text{const}$ is the reference travel distance. The antenna locations in the slant coordinates are $\mathbf{x}^{(1)} = (-R + x_u^{(1)}, x_v^{(1)})$ and $\mathbf{x}^{(2)} = (-R + x_u^{(2)}, x_v^{(2)})$. This setup removes the asymmetry pointed out in item 5 of Section 4. We also consider two point scatterers \mathbf{z}_a and \mathbf{z}_b .

We will assume that both antennas are located near \mathbf{R} while both scatterers are near \mathbf{T} (see Fig. 4) so that

$$\frac{|\mathbf{x}^{(1)} - \mathbf{R}|}{R} \sim \varepsilon, \quad \frac{|\mathbf{x}^{(2)} - \mathbf{R}|}{R} \sim \varepsilon, \quad \frac{|\mathbf{z}_a|}{R} \sim \varepsilon, \quad \frac{|\mathbf{z}_b|}{R} \sim \varepsilon,$$

where $\varepsilon \ll 1$ is a small parameter (cf. (5)). Applying the Taylor expansion to the Pythagorean formula, we approximately calculate the travel distances:

$$(63) \quad \begin{aligned} \frac{R_{\mathbf{z}_a}^{(1)}}{R} &= 1 + \frac{z_{ua} - x_u^{(1)}}{R} + \frac{(z_{va} - x_v^{(1)})^2}{2R^2} + \mathcal{O}(\varepsilon^3), \\ \frac{R_{\mathbf{z}_a}^{(2)}}{R} &= 1 + \frac{z_{ua} - x_u^{(2)}}{R} + \frac{(z_{va} - x_v^{(2)})^2}{2R^2} + \mathcal{O}(\varepsilon^3), \end{aligned}$$

and similarly for $R_{\mathbf{z}_b}^{(1)}$ and $R_{\mathbf{z}_b}^{(2)}$ that correspond to the scatterer at $\mathbf{z}_b = (z_{ub}, z_{vb})$.

It is important to estimate the truncated part in formulae (63) because, as we saw in item 3 of Section 4, the linearized expression (7) may be insufficiently accurate. Consider a spaceborne radar with $R \sim 10^3 \text{ km}$ and take, say, $\varepsilon = 10^{-3}$. This allows for the baseline $|\mathbf{x}^{(2)} - \mathbf{x}^{(1)}|$ and scene size $\max |\mathbf{z}|$ of up to 1 km , which is acceptable for both quantities. Then, the terms neglected in (63) are $\sim R\varepsilon^3 \sim 1 \text{ mm}$, i.e., much smaller than the wavelength.

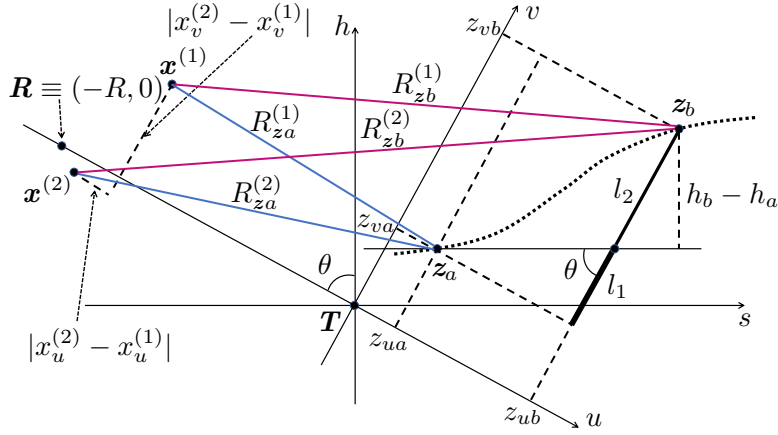


FIGURE 4. Radar interferometry with two coequal antennas. All coordinates are specified in the slant reference frame (u, v) . To illustrate formula (88), note that $l_1 + l_2 = z_{vb} - z_{va}$.

Let $R_{ya}^{(1)}$ and $R_{ya}^{(2)}$ be the focusing distances close to $R_{za}^{(1)}$ and $R_{za}^{(2)}$, respectively, in the sense of (51). According to Section 5.1, we build the interferogram as follows (see (59)):

$$(64) \quad q_a = \overline{\mathcal{I}^{(1)}(R_{ya}^{(1)})} \mathcal{I}^{(2)}(R_{ya}^{(2)}),$$

where neither $\mathcal{I}^{(1)}(R_{ya}^{(1)})$ nor $\mathcal{I}^{(2)}(R_{ya}^{(2)})$ are supposed to have any other contributions besides those from z_a . Then, we substitute (63) into (57) and (64) and dropping the $\mathcal{O}(\varepsilon^3)$ terms derive the phase of the interferogram:

$$(65) \quad \psi_a = \angle q_a = 2k(R_{za}^{(2)} - R_{za}^{(1)}) = \Phi_q - 2kz_{va} \frac{x_v^{(2)} - x_v^{(1)}}{R},$$

where

$$(66) \quad \Phi_q = 2k \left(-(x_u^{(2)} - x_u^{(1)}) + \frac{(x_v^{(2)})^2 - (x_v^{(1)})^2}{2R} \right).$$

The interferogram q_a in (65) is the data, and it is essential to remember that the real and imaginary part of each of the two images in (64) are two independent values determined from the antenna measurements, see Section 3.2. For a complex number defined this way, its complex phase is known only accurate to an additive term of $2\pi n$, where n is integer. For example, we can assume that $|\psi_a| < \pi$. On the right-hand side of (65), only the last term depends on z_a , while Φ_q is determined by the antenna coordinates $\mathbf{x}^{(1)}$ and $\mathbf{x}^{(2)}$ that may contain errors much larger than the wavelength (see item 2 in Section 4):

$$(67) \quad (x_u^{(2)} - x_u^{(1)}) = (x_u^{(2)} - x_u^{(1)})^{(\text{exact})} + \eta, \quad \text{where } |\eta| \gg \lambda = \frac{2\pi}{k}.$$

Substituting (67) into (66), we get:

$$(68) \quad \Phi_q = \Phi_q^{(\text{exact})} + \phi, \quad \text{where } |\phi| \gg \pi.$$

Consequently, the error ϕ due to Φ_q could be much larger than the magnitude of the data ψ_a , which makes the accurate determination of z_{va} from equation (65) impossible.

However, we can cancel Φ_q and reduce the effect of the corresponding errors by considering another point scatterer located at $\mathbf{z}_b = (z_{ub}, z_{vb})$, such that (cf. (62))

$$(69) \quad |R_{z_a}^{(1)} - R_{z_b}^{(1)}| \gg \Delta_R \quad \text{and} \quad |R_{z_a}^{(2)} - R_{z_b}^{(2)}| \gg \Delta_R.$$

The separation (69) yields both interferograms, q_a and q_b , in the form (64), as per the discussion in Section 5.1. Then, computing ψ_b as in (65) and subtracting ψ_a from it:

$$(70) \quad \frac{\psi_b - \psi_a}{2k} = (R_{z_b}^{(2)} - R_{z_b}^{(1)}) - (R_{z_a}^{(2)} - R_{z_a}^{(1)}) = -\frac{x_v^{(2)} - x_v^{(1)}}{R}(z_{vb} - z_{va}).$$

The term $x_v^{(2)} - x_v^{(1)}$ on the right-hand side of (70) is prone to the same absolute errors as in (67). However, their magnitude as compared to the wavelength no longer matters because

$$(71) \quad z_{vb} - z_{va} = -R \frac{\psi_b - \psi_a}{2k} \frac{1}{x_v^{(2)} - x_v^{(1)}},$$

and the relative error on the right-hand side of (71) will obviously be $\sim \frac{|\eta|}{|x_v^{(2)} - x_v^{(1)}|}$. This addresses the role of inaccuracies in antenna position, as per item 2 of Section 4.

A counterpart of (71) in the traditional framework is formula (12) of Section 2. However, for (71) to hold, we require the separation (69) so as to avoid the possible degeneration that may lead to missing data for elevation retrieval in (12). This addresses item 4 of Section 4.

It is easy to see that conditions $|\psi_a| < \pi$ and $|\psi_b| < \pi$ (see the discussion following (66)) also impose a restriction on the range of reconstructed values of $z_{vb} - z_{va}$ in (71). We discuss this problem in Section 5.4.

5.3. Removal of flat Earth phase. In topographic applications of radar interferometry, the topographical height h as a function of the horizontal coordinates is reconstructed from the received radar signals. Formula (70) allows one to use the interferogram to obtain the cross-slant distance between the two point scatterers, $z_{vb} - z_{va}$. This, however, is not sufficient for deriving $h = h(s)$. Indeed, considering the relation between the upright (s, h) and slanted (z_u, z_v) coordinates,

$$(72) \quad \begin{aligned} h &= z_v \sin \theta - z_u \cos \theta, \\ s &= z_v \cos \theta + z_u \sin \theta, \end{aligned}$$

we can recast the top line of (72) for two scatterers, a and b , as follows:

$$(73) \quad h_b - h_a = (z_{vb} - z_{va}) \sin \theta - (z_{ub} - z_{ua}) \cos \theta.$$

For height retrieval, only the term $(z_{vb} - z_{va})$ on the right-hand side of (73) can be derived immediately from the interferometric data, see (71). Yet to obtain the height information, we have to evaluate the term $(z_{ub} - z_{ua})$ as well. This can be done by dropping the quadratic terms in (63) and using the focusing parameters, for example:

$$(74) \quad (z_{ub} - z_{ua}) \approx (R_{z_b}^{(1)} - R_{z_a}^{(1)}) \approx (R_{y_b}^{(1)} - R_{y_a}^{(1)}),$$

see Fig. 4. Then, formula (73) becomes:

$$(75) \quad \begin{aligned} h_b - h_a &\approx -\frac{\psi_b - \psi_a}{2k\Delta\theta} \sin \theta - (R_{yb}^{(1)} - R_{ya}^{(1)}) \cos \theta \\ &= -\frac{\sin \theta}{2k\Delta\theta} \left((\psi_b - \psi_a) - \underbrace{\frac{2k\Delta\theta(R_{ya}^{(1)} - R_{yb}^{(1)})}{\tan \theta}}_{\text{flat Earth phase}} \right), \end{aligned}$$

where $\Delta\theta = (x_v^{(2)} - x_v^{(1)})/R$. The flat Earth phase in (75) was previously introduced in equation (14).

Note that unlike for deriving (70), dropping the $\mathcal{O}(\varepsilon^2)$ terms in (63) to obtain (74) is acceptable. Indeed, according to (51), the second approximation in (74) introduces the error of about the resolution size:

$$|R_{yb}^{(1)} - R_{zb}^{(1)}| + |R_{ya}^{(1)} - R_{za}^{(1)}| \sim \Delta_R.$$

For an X-band system with $\omega_0 = 2\pi \cdot 10\text{GHz}$ ($\lambda = 3\text{cm}$) and $B/\omega_0 = 1\%$, we have $\Delta_R \approx 1.5\text{m}$, see (50). At the same time, with $R \sim 10^3\text{km}$ and $\varepsilon = 10^{-3}$, the quadratic terms in (63) are $\sim \frac{1}{2}R\varepsilon^2 \sim 0.5\text{m}$, i.e., three times smaller than Δ_R . Thus, approximation (74) may introduce the total error of about Δ_R into the calculated elevation. Clearly, antenna 2 could have been used instead of antenna 1 for obtaining the approximation (74) and computing the elevation (75).

Another way to eliminate the term $(z_{ub} - z_{ua})$ from (73) is to adjust the carrier frequencies of the two satellites (cf. formula (16)). Accordingly, we extend the framework of Section 5.2 to the case where the wavenumbers k_1 and k_2 of the two imaging systems are related by

$$(76) \quad k_1 \sin \theta_1 = k_2 \sin \theta_2.$$

In formula (76),

$$\theta_1 \approx \theta - \frac{x_v^{(1)}}{R} \quad \text{and} \quad \theta_2 \approx \theta - \frac{x_v^{(2)}}{R}$$

are the incidence angles for antennas 1 and 2, respectively. We are aiming to satisfy (76) with first order in ε , while for phase calculations we will still be using formulae (63) that are quadratic in ε . To symmetrize relation (18), we introduce

$$(77) \quad \Delta\theta = \frac{x_v^{(2)} - x_v^{(1)}}{R}, \quad \Delta k = k \frac{\Delta\theta}{\tan \theta},$$

so that given $|\Delta\theta| \sim \varepsilon \ll 1$ and $|\Delta k| \ll k$, condition (76) is satisfied for

$$(78) \quad k_1 = k - \frac{\Delta k}{2}, \quad k_2 = k + \frac{\Delta k}{2}.$$

In actual systems, rather than changing the carrier frequencies, one can extract two sub-bands of the original frequency band $[\omega_0 - \frac{B}{2}, \omega_0 + \frac{B}{2}]$ (see formulae (26), (27)):

$$(79a) \quad \left[\omega_1 - \frac{\tilde{B}}{2}, \omega_1 + \frac{\tilde{B}}{2} \right] \quad \text{and} \quad \left[\omega_2 - \frac{\tilde{B}}{2}, \omega_2 + \frac{\tilde{B}}{2} \right],$$

where

$$(79b) \quad \omega_1 = k_1 c \quad \text{and} \quad \omega_2 = k_2 c,$$

and

$$(79c) \quad \tilde{B} = B - |\Delta k|c.$$

The condition $\tilde{B} > 0$ requires

$$(79d) \quad |\Delta k| < B/c \quad \Leftrightarrow \quad |\omega_1 - \omega_2| < B.$$

To generate a sub-band image using the chirp (25)–(27), one applies a modified matched filter $\tilde{P}_{\text{filt}}(t, \mathbf{y})$. If $\omega_0 < \omega_1 < \omega_0 + \frac{B}{2}$, this filter is given by (cf. formulae (35), (36)):

$$(80) \quad \tilde{P}_{\text{filt}}(t, \mathbf{y}) = e^{i\tilde{\Phi}} \chi_{\tilde{\tau}}(t - \tilde{t}_{\mathbf{y}}) e^{i\omega_1(t - \tilde{t}_{\mathbf{y}}) + i\alpha(t - \tilde{t}_{\mathbf{y}})^2},$$

where

$$\tilde{\tau} = \tau - \frac{\omega_1 - \omega_0}{\alpha}, \quad \tilde{t}_{\mathbf{y}} = \frac{2R_{\mathbf{y}}}{c} + \frac{\omega_1 - \omega_0}{2\alpha}, \quad \tilde{\Phi} = \frac{\omega_0^2 - \omega_1^2}{4\alpha}.$$

Application of the filter (80) to signal (48) results in (cf. equation (49)):

$$(81) \quad \tilde{I}^{(1)}(R_{\mathbf{y}}^{(1)}; k_1) = \nu_0 \cdot \tilde{\tau} e^{-2ik_1(R_{\mathbf{y}}^{(1)} - R_z^{(1)})} \text{sinc}\left(\tilde{B} \frac{R_{\mathbf{y}}^{(1)} - R_z^{(1)}}{c}\right).$$

The image $\tilde{I}^{(2)}(\mathbf{y})$ is built similarly, but using the second sub-band in (79a). Then, defining

$$(82) \quad \tilde{\mathcal{I}}^{(1)}(R_{\mathbf{y}}^{(1)}; k_1) = \tilde{I}^{(1)}(R_{\mathbf{y}}^{(1)}; k_1) e^{2ik_1 R_{\mathbf{y}}^{(1)}} \quad \text{and} \quad \tilde{\mathcal{I}}^{(2)}(R_{\mathbf{y}}^{(2)}; k_2) = \tilde{I}^{(2)}(R_{\mathbf{y}}^{(2)}; k_2) e^{2ik_2 R_{\mathbf{y}}^{(2)}}$$

as in (56), we construct the interferograms as follows (cf. equation (64)):

$$(83) \quad \tilde{q}_a = \overline{\tilde{\mathcal{I}}^{(1)}(R_{\mathbf{y}_a}^{(1)}; k_1)} \tilde{\mathcal{I}}^{(2)}(R_{\mathbf{y}_a}^{(1)}; k_2) \quad \text{and} \quad \tilde{q}_b = \overline{\tilde{\mathcal{I}}^{(1)}(R_{\mathbf{y}_b}^{(1)}; k_1)} \tilde{\mathcal{I}}^{(2)}(R_{\mathbf{y}_b}^{(1)}; k_2).$$

For interferogram phases, we obtain from (83) using (63), (65), (66), (77), and (78):

$$(84a) \quad \begin{aligned} \tilde{\psi}_a &= \angle \tilde{q}_a = 2(k_2 R_{z_a}^{(2)} - k_1 R_{z_a}^{(1)}) = 2k(R_{z_a}^{(2)} - R_{z_a}^{(1)}) + \Delta k(R_{z_a}^{(2)} + R_{z_a}^{(1)}) \\ &= \psi_a + \Delta k(R_{z_a}^{(2)} + R_{z_a}^{(1)}) = \Phi_q + \Delta k(2R + 2z_{ua} - x_u^{(1)} - x_u^{(2)}) - 2k\Delta\theta z_{va} \end{aligned}$$

and

$$(84b) \quad \begin{aligned} \tilde{\psi}_b &= \angle \tilde{q}_b = 2(k_2 R_{z_b}^{(2)} - k_1 R_{z_b}^{(1)}) = 2k(R_{z_b}^{(2)} - R_{z_b}^{(1)}) + \Delta k(R_{z_b}^{(2)} + R_{z_b}^{(1)}) \\ &= \psi_b + \Delta k(R_{z_b}^{(2)} + R_{z_b}^{(1)}) = \Phi_q + \Delta k(2R + 2z_{ub} - x_u^{(1)} - x_u^{(2)}) - 2k\Delta\theta z_{vb} \end{aligned}$$

(cf. equation (17)). Note that in (84), we have dropped the $\mathcal{O}(\varepsilon^2)$ terms in the expansions of all distances when multiplied by Δk , because $|\Delta k|/k \sim \varepsilon$, see (77). Similarly to (65), formulae (84) contain large phase errors due to the terms

$$(85) \quad \Phi_q + \Delta k(2R - x_u^{(1)} - x_u^{(2)}).$$

These errors can be expressed as in (67), (68). Moreover, similarly to (70), we can reduce these errors by taking the difference between the two phases, i.e., subtracting $\tilde{\psi}_a$ from $\tilde{\psi}_b$:

$$(86) \quad \tilde{\psi}_b - \tilde{\psi}_a = 2\Delta k(z_{ub} - z_{ua}) - 2k\Delta\theta(z_{vb} - z_{va}).$$

Substituting (77) and (72) into (86), we obtain:

$$(87) \quad \frac{\tilde{\psi}_b - \tilde{\psi}_a}{2k} = -\Delta\theta \left((z_{vb} - z_{va}) - \frac{z_{ub} - z_{ua}}{\tan\theta} \right).$$

With the help of Fig. 4, we can see that

$$(88) \quad z_{vb} - z_{va} = l_1 + l_2, \quad \text{where} \quad l_1 = \frac{z_{ub} - z_{ua}}{\tan\theta}, \quad l_2 = \frac{h_b - h_a}{\sin\theta}.$$

Thus, (87) simplifies to

$$(89) \quad \frac{\tilde{\psi}_b - \tilde{\psi}_a}{2k} = -\Delta\theta \frac{h_b - h_a}{\sin\theta}.$$

Formula (89) corresponds to formula (24) of Section 2 (see also Section 5.4).

In (89), unlike in (75), the difference of interferometric phases $\tilde{\psi}_b - \tilde{\psi}_a$ is related to the scatterer coordinates via only the elevation difference $h_b - h_a$. Thus, we have demonstrated once again that the procedure of adjusting the wavenumbers (76) removes the flat Earth phase from the interferogram, circumventing the need for approximation (74). This, however, comes at a price of not using the entire signal bandwidth (note \tilde{B} instead of B under the sinc in (81)), and since $\tilde{B} < B$, see (79c), the resolution size Δ_R increases, see (50). As the two scatterers a and b have to be sufficiently far apart, see (69), the deterioration of resolution also reduces the quality of the elevation map obtained with the help of (89), because the quantity $h_b - h_a$ is attributed to a pair of locations. Besides, the sub-band processing by the filter (80) is only possible if condition (79d) is satisfied, while the interferometric formulation of Section 5.2 is free from this limitation.

In Section 6, we will discuss the extended scatterers and revisit the procedure of adjusting the incident wavenumbers once again (see Section 6.3). This will address item 6 of Section 4.

5.4. Phase unwrapping. Application of formulae (12), (24), (75), or (89) (as well as (113) in Section 6) to experimental data has a limitation due to the 2π -ambiguity of the complex phase of the interferogram (see the discussion following (66)). In terms of the scatterer elevation, this corresponds to the following condition in (75) and (89):

$$(90) \quad |h_b - h_a| < \pi \frac{\sin\theta}{2k\Delta\theta} = \frac{\lambda \sin\theta}{4\Delta\theta}.$$

The threshold on the right-hand side of (90) is half of what is known as height ambiguity (i.e., the change in elevation that yields the variation of interferometric phase by 2π , see, e.g., [32, 24]). To measure the elevation increments exceeding this threshold, one should be able to extend the interferogram phase $\psi(\mathbf{y}) = \angle q(\mathbf{y})$ beyond the interval $[-\pi, \pi]$ by adding multiples of 2π for certain values of \mathbf{y} . This procedure is called phase unwrapping. We do not consider it in this work and refer the reader to [16, 31, 27] instead. Many phase unwrapping techniques originate from the ideas formulated in [21]. These methods rely on smoothness of the interferogram $q = q(\mathbf{y})$ given by (64), $\mathbf{y} \in \mathbb{R}^2$, so that jumps in its complex phase equal to $\pm 2\pi$ can be identified and removed from the experimental data.

6. Interferometry for δ -correlated extended scatterers. In this section, we analyze the interferometric height reconstruction in the case of extended scatterers. Such scatterers are characterized by reflectivity functions with non-singular support (unlike in (47)). An important feature observed in actual radar images of extended targets is speckle, i.e., strong and rapid variations of the amplitude and phase of the image, which are due to the coherent nature of SAR imaging [22, 33]. An object exhibiting speckle can often be thought of as a collection of individual point scatterers that cannot be separated by the system due to its finite resolution size. The corresponding phenomenological model of SAR imaging with speckle involves interpreting $\nu(\mathbf{z})$ as a random field with certain autocorrelation properties. Then,

the image $I(\mathbf{y})$, interferogram $q(\mathbf{y})$, and its phase $\psi(\mathbf{y}) = \angle q(\mathbf{y})$, become random as well.

When the interferometry of extended scatterers is considered, equations (56)–(58) acquire extra terms due to the aforementioned additional scatterers. These terms can be thought of as noise that is called the baseline, or geometric, decorrelation: the interferogram becomes more noisy as the angle between the incident directions $\Delta\theta$ increases, as will be seen from (108). Due to the same limitations on resolution that are responsible for speckle, the return from unwanted scatterers cannot be selectively suppressed. Still, the extent of this decorrelation can be reduced by the wavenumber adjustment procedure that involves the imaging operator (40), as demonstrated in Section 6.3. In the case of baseline decorrelation, this allows one to use larger values of $\Delta\theta$, which may be beneficial because it improves the sensitivity of the interferometer, i.e., reduces $|h_b - h_a|$ for the same $|\tilde{\psi}_b - \tilde{\psi}_a|$, see (89).

Controlling the level of interferogram noise² is essential not only because it introduces random errors into the resulting elevations. Keeping the noise low is critical since the phase unwrapping procedure mentioned in Section 5.4 relies on smoothness of the interferogram. In reality, the experimentally obtained values of $q(\mathbf{y})$ are given on a discrete grid and contain noise. Excessive amount of noise in the interferogram may hamper one's ability to unwrap its phase and derive the height information from the interferogram.

The relation between the randomness of the interferogram and the convolution-based imaging operator presented in Section 3.1 is widely acknowledged in the literature [42]. At the same time, full understanding of the origin of different terms in the interferogram still requires a detailed analysis of the imaging geometry, similarly to the case of individual point scatterers presented in Section 5. Additionally, comparing the treatment of deterministic and stochastic cases in the same framework helps explain the differences between the two approaches to the flat Earth phase removal mentioned in item 6 of Section 4.

6.1. Interferogram and interferometric coherence. We will model the reflectivity $\nu(\mathbf{z})$ of an extended scatterer by a δ -correlated circular Gaussian random field [33]:

$$(91) \quad \langle \overline{\nu(\mathbf{z}')} \nu(\mathbf{z}) \rangle = \sigma^2(\mathbf{z}) \delta(\mathbf{z}' - \mathbf{z}),$$

where $\langle \dots \rangle$ denotes statistical averaging. Representation (91) turns the scattered field (34) and radar image (37) into random functions as well.

A counterpart of the deterministic interferogram (64) for an extended scatterer is

$$(92) \quad Q(\mathbf{y}) = \left\langle \overline{\mathcal{I}^{(1)}(R_{\mathbf{y}}^{(1)})} \mathcal{I}^{(2)}(R_{\mathbf{y}}^{(2)}) \right\rangle,$$

and the complex coherence is defined as

$$(93) \quad \gamma(\mathbf{y}) = \frac{Q(\mathbf{y})}{\left(\left\langle |\mathcal{I}^{(1)}(R_{\mathbf{y}}^{(1)})|^2 \right\rangle \left\langle |\mathcal{I}^{(2)}(R_{\mathbf{y}}^{(2)})|^2 \right\rangle \right)^{1/2}}.$$

In formulae (92) and (93),

$$R_{\mathbf{y}}^{(1)} = |\mathbf{y}^{(1)} - \mathbf{x}^{(1)}|, \quad R_{\mathbf{y}}^{(2)} = |\mathbf{y}^{(2)} - \mathbf{x}^{(2)}|,$$

²The sources of interferogram noise include the scatterer itself, as well as the signal processing procedure, receiver noise, and irregularities of the propagation medium.

and similarly to Section 5.1, the focusing parameters $\mathbf{y}^{(1)}$ and $\mathbf{y}^{(2)}$ for the two antennas can be different due to co-registration errors, see (53). The argument \mathbf{y} of the interferogram $Q(\mathbf{y})$ can be associated with either of the two focusing parameters.

In practice, statistical averaging in (92) and (93) is replaced with spatial averaging under the assumption of ergodicity:

$$(94) \quad \begin{aligned} Q^{\text{exper}}(\mathbf{y}) &= \frac{1}{N} \sum_{j=1}^N \overline{\mathcal{I}^{(1)}(\mathbf{y}_j)} \mathcal{I}^{(2)}(\mathbf{y}_j), \\ \gamma^{\text{exper}}(\mathbf{y}) &= \frac{Q^{\text{exper}}(\mathbf{y})}{\left(\frac{1}{N} \sum_{j=1}^N |\mathcal{I}^{(1)}(\mathbf{y}_j)|^2\right)^{1/2} \left(\frac{1}{N} \sum_{j=1}^N |\mathcal{I}^{(2)}(\mathbf{y}_j)|^2\right)^{1/2}}, \end{aligned}$$

where j enumerates sampling locations in a neighborhood of \mathbf{y} . Smaller absolute values of coherence $|\gamma|$, see (93), correspond to more noise in the experimentally computed interferogram (94). In particular, the following inequality sets the lower bound for the variance of the interferogram phase (see, e.g., [28, 1], [8, Section A.3], and [24, Section 4.2.2]):

$$(95) \quad \text{Var}(\angle Q^{\text{exper}}(\mathbf{y})) \equiv \langle (\angle Q^{\text{exper}}(\mathbf{y}))^2 \rangle - (\angle Q(\mathbf{y}))^2 > \frac{1 - \gamma(\mathbf{y})^2}{2N\gamma(\mathbf{y})^2}.$$

With the help of (40), (41), (56), and (91), we obtain the following expression for the interferogram of an extended scatterer:

$$(96) \quad \begin{aligned} Q(\mathbf{y}) &= e^{2ik(R_y^{(2)} - R_y^{(1)})} \int \overline{W(R_y^{(1)} - R_z^{(1)})} W(R_y^{(2)} - R_z^{(2)}) \sigma^2(\mathbf{z}) \, d\mathbf{z} \\ &= \int e^{2ik(R_z^{(2)} - R_z^{(1)})} \overline{V(R_y^{(1)} - R_z^{(1)})} V(R_y^{(2)} - R_z^{(2)}) \sigma^2(\mathbf{z}) \, d\mathbf{z}, \end{aligned}$$

where $V(l) \equiv \tau \text{sinc}(Bl/c)$ is the envelope (i.e., slow part) of $W(l)$ given by (41). For the exponential function under the second integral in (96), we can write using (63) and (77):

$$e^{2ik(R_z^{(2)} - R_z^{(1)})} \approx \text{const}(\mathbf{z}) \cdot e^{2ikz_v(x_v^{(1)} - x_v^{(2)})/R} = \text{const}(\mathbf{z}) \cdot e^{-4\pi iz_v \Delta\theta/\lambda}.$$

Since $|\Delta\theta| \ll 1$, we can keep only the leading terms w.r.t. ε in the arguments of V :

$$(97a) \quad V(R_y^{(1)} - R_z^{(1)}) \approx V(y_u^{(1)} - z_u), \quad V(R_y^{(2)} - R_z^{(2)}) \approx V(y_u^{(2)} - z_u).$$

Furthermore, we will use the same ‘‘focusing slant coordinate’’ y_u in the slow factors for the two radar systems, so that both envelopes are approximated as follows (see Fig. 5):

$$(97b) \quad V(y_u^{(1)} - z_u) \approx V(y_u^{(2)} - z_u) \approx V(y_u - z_u),$$

For sufficiently accurate co-registration, see (53), the corresponding error in the argument of the sinc function is small. Changing the variables (see Fig. 5):

$$(98) \quad (z_u, z_v) \longrightarrow (z'_u, h) \equiv (z_u - y_u, h),$$

where h is given by (72), so that $d\mathbf{z} = dz'_u dh / \sin\theta$, we transform (96) into (99)

$$Q(y_u) = \frac{\tau^2}{\sin\theta} e^{i\Phi_Q} \int e^{-2ik \frac{\Delta\theta}{\sin\theta} h} \left(\int \sigma^2(z'_u, h) \text{sinc}^2\left(\frac{Bz'_u}{c}\right) e^{-2ik \frac{\Delta\theta}{\tan\theta} z'_u} dz'_u \right) dh,$$

where

$$(100) \quad \Phi_Q = \Phi_q - 2ky_u \frac{\Delta\theta}{\tan\theta} \equiv \Phi_q + \Phi_{\text{fEP}}(y_u),$$

and the dependence of the right-hand side of (99) on y_u is via z'_u , see (98). The term Φ_q in formula (100) describes the ambiguity of the phase and is the same as (66), while $\Phi_{\text{fEP}}(y_u) = -2k\Delta\theta y_u / \tan\theta$ accounts for the flat Earth phase (cf. (75)).

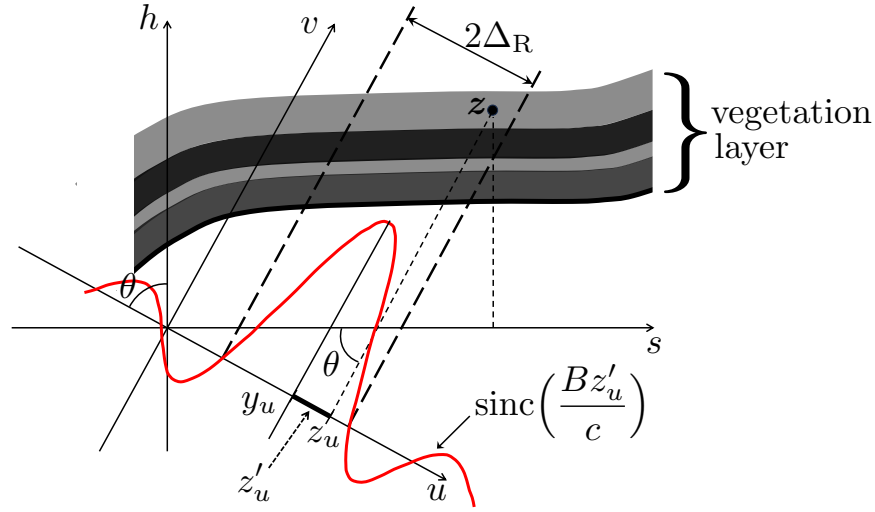


FIGURE 5. Interferometry of an extended vertically stratified scatterer. In the analysis of (106), $V(z'_u) = \tau \text{sinc}(Bz'_u/c)$ is considered as a function of $z_u = y_u + z'_u$ (cf. Fig. 3).

In geophysical applications, one often considers

$$(101) \quad \sigma^2(\mathbf{z}) \equiv \sigma^2(s, h) = \sigma_h^2(h)\sigma_s^2(s),$$

where (cf. equations (72) and (98))

$$s = s(z'_u, h) = \frac{h}{\tan\theta} + \frac{z_u}{\sin\theta} = \frac{h}{\tan\theta} + \frac{y_u + z'_u}{\sin\theta}.$$

In formula (101), $\sigma_h^2(h)$ represents the vertical structure of the vegetation layer and $\sigma_s^2(s)$ accounts for the variation in the horizontal direction. The characteristic scale of the latter is assumed much larger than that of the former, as well as than Δ_R , see Fig. 5. Then,

$$(102) \quad \sigma_s^2(s) \equiv \sigma_s^2(s(z'_u, h)) \approx \sigma_s^2(y_u / \sin\theta),$$

and the two integrals in (99) separate:

$$(103) \quad Q(y_u) = \frac{\tau^2}{\sin\theta} e^{i\Phi_Q} \sigma_s^2(y_u / \sin\theta) \int \sigma_h^2(h) e^{-2ik \frac{\Delta\theta}{\sin\theta} h} dh \cdot \int \text{sinc}^2\left(\frac{Bz'_u}{c}\right) e^{-2ik \frac{\Delta\theta}{\tan\theta} z'_u} dz'_u.$$

For the denominator in the definition (93) of the coherence γ , we assume:

$$\left\langle |\mathcal{I}^{(1)}(R_y^{(1)})|^2 \right\rangle \approx \left\langle |\mathcal{I}^{(2)}(R_y^{(2)})|^2 \right\rangle,$$

because the imaging conditions for the two antennas are nearly identical. Thus, to compute the denominator, we can repeat the procedure of (96)–(103) assuming $R_y^{(1)} = R_y^{(2)}$ and $R_z^{(1)} = R_z^{(2)}$. Then, the coherence γ factors into a product of the volumetric and geometric terms:

$$(104) \quad \gamma = \gamma^{\text{vol}} \gamma^{\text{geom}},$$

where

$$(105) \quad \gamma^{\text{vol}} = e^{i\Phi_Q} \frac{\int \sigma^2(h) e^{-2ik \frac{\Delta\theta}{\sin\theta} h} dh}{\int \sigma^2(h) dh}$$

and

$$(106) \quad \gamma^{\text{geom}} = \frac{\int \text{sinc}^2\left(\frac{Bz'_u}{c}\right) e^{-2ik \frac{\Delta\theta}{\tan\theta} z'_u} dz'_u}{\int \text{sinc}^2\left(\frac{Bz'_u}{c}\right) dz'_u}.$$

Formulae (105) and (106) highlight the differences between the interferometry of point scatterers and extended scatterers. In the expression (105) for γ^{vol} , the elevation-dependent phase (cf. (70)) is calculated for a range of elevations and weighted with $\sigma_h^2(h)$. In turn, under assumptions (102), the numerator of expression (106) for γ^{geom} contains the flat Earth phase (cf. (75)) weighted with the square of the point spread function $V(z'_u)$, see (41).

6.2. Height retrieval for a vertically localized distributed scatterer. If the scatterer is localized in the vertical coordinate:

$$(107) \quad \sigma_h^2(h) = \sigma_0^2 \delta(h - h_0)$$

(this form is used to represent the reflectivity of a hard surface, e.g., bare soil, at elevation h_0), then formula (105) yields $\gamma^{\text{vol}} = e^{i\Phi_Q} e^{-2ikh_0 \frac{\Delta\theta}{\sin\theta}}$. Hence, there is no decorrelation due to the vertical structure of the scatterer (107): $|\gamma^{\text{vol}}| = 1$.

The term γ^{geom} yields decorrelation even in the case (107). Indeed, using

$$\int \text{sinc}^2(\alpha\kappa) e^{i\kappa x} d\kappa = \frac{\pi}{\alpha} \text{tri} \frac{x}{2\alpha},$$

where the triangle function is defined as

$$\text{tri} x = \begin{cases} 1 - |x|, & |x| \leq 1, \\ 0, & \text{otherwise,} \end{cases}$$

we calculate γ^{geom} according to (106) and obtain:

$$(108) \quad \gamma^{\text{geom}} = \text{tri} \left(\frac{\omega_0}{B} \frac{\Delta\theta}{\tan\theta} \right).$$

Altogether, for the vertically localized scatterer (107), we have:

$$(109) \quad \gamma = e^{i\Phi_Q} e^{-2ikh_0 \frac{\Delta\theta}{\sin\theta}} \text{tri} \left(\frac{\omega_0}{B} \frac{\Delta\theta}{\tan\theta} \right).$$

Expressions (108) and (109) demonstrate a well-known effect of geometric decorrelation in surface scattering [42]:

$$|\gamma| = \text{tri} \left(\frac{\omega_0}{B} \frac{\Delta\theta}{\tan\theta} \right).$$

Namely, to keep the two radar images correlated, one must ensure $|\gamma| > 0$, which sets the upper bound for the interferometric angle $\Delta\theta$:

$$(110) \quad \frac{\omega_0 |\Delta\theta|}{B \tan \theta} \leq 1 \Leftrightarrow |\Delta\theta| \leq \frac{B}{\omega_0} \tan \theta.$$

At the same time, as long as condition (110) is satisfied, we have $\angle\gamma = \angle\gamma^{\text{vol}}$ because $\angle\gamma^{\text{geom}} = 0$. In turn, formula (105) indicates that γ^{vol} contains an elevation-dependent phase that can be used in the interferometric elevation retrieval, similarly to the case of isolated point scatterers considered in Sections 2 and 5.

The procedure for height retrieval from the interferogram (92) (or (94)) is similar to that for point scatterers. To enable variation of surface elevation, we introduce a slow dependence of h_0 in (107) on the slant coordinate: $h_0 \rightarrow h_0(z_u)$. In other words, we will assume that h_0 is constant on the scale of up to

$$(111) \quad \max_{j,j'} |\mathbf{y}_j - \mathbf{y}_{j'}| \gg \Delta_R,$$

where \mathbf{y}_j and $\mathbf{y}_{j'}$ are the sampling points in the averaging procedure (94), but allow h_0 to vary on larger scales of its argument. Then, formulae (100) and (105) yield:

$$(112) \quad \angle\gamma(y_u) = \angle\gamma^{\text{vol}}(y_u) = \Phi_q - 2ky_u \frac{\Delta\theta}{\tan \theta} - 2k \frac{\Delta\theta}{\sin \theta} h_0(y_u),$$

where we can write $h_0 = h_0(y_u)$ because h_0 is constant on the scale (111). Similarly to Section 5.2, we take two values of the coordinate, y_{ua} and y_{ub} , such that $|y_{ub} - y_{ub}| \gg \max |\mathbf{y}_j - \mathbf{y}_{j'}|$. The term Φ_q is eliminated by subtracting the two phases from one another (cf. equation (70)):

$$\begin{aligned} \angle\gamma(y_{ub}) - \angle\gamma(y_{ua}) &= -2k\Delta\theta \frac{y_{ub} - y_{ua}}{\tan \theta} - 2k\Delta\theta \frac{h_0(y_{ub}) - h_0(y_{ua})}{\sin \theta} \\ &= \Phi_{\text{fEP}}(y_{ub}) - \Phi_{\text{fEP}}(y_{ua}) - 2k\Delta\theta \frac{h_0(y_{ub}) - h_0(y_{ua})}{\sin \theta}. \end{aligned}$$

Then, the difference in elevations can be expressed as follows (cf. formula (75)):

$$(113) \quad h_0(y_{ub}) - h_0(y_{ua}) = -\frac{\sin \theta}{2k\Delta\theta} \left((\angle\gamma(y_{ub}) - \angle\gamma(y_{ua})) - (\Phi_{\text{fEP}}(y_{ub}) - \Phi_{\text{fEP}}(y_{ua})) \right).$$

Finally, the flat Earth phase terms Φ_{fEP} on the right-hand side of (113) can be explicitly computed according to (100) (see also Section 5.4).

For the interferometry of isolated point scatterers (Section 5.1), the key relation (58) was obtained from the point scatterer model (47) provided that this scatterer was sufficiently isolated, see (62). Similarly, formulae (112) and (113) are derived under several assumptions about the extended scatterer, including (91), (101), (107), and the properties of $h_0(z_u)$. These two scatterer models can be thought of as opposite extremes from the standpoint of the horizontal localization of the scatterer. Yet for each of them, the sensitivity of the resulting interferogram to focusing coordinates, registration and trajectory errors, etc., appears low (see Section 4). Other scatterer models can also be used for the analysis of radar interferometry [30, 20, 17, 26], but they are considerably less common.

While formula (113) allows one to find the difference in elevations via $\angle\gamma = \angle\gamma^{\text{vol}}$, the term γ^{geom} in (104) increases the variance of the result, as described by (95). This has a detrimental effect on interferometric performance. The geometric decorrelation is reduced if the scatterer is localized in both the vertical and horizontal

direction. For example, if we take $\sigma_h^2(h)$ as in (107) and

$$(114) \quad \sigma_s^2(s) \sim e^{-(s-s_0)^2/r^2}, \quad \text{where } \lambda \ll r \ll c/B,$$

(which contradicts the earlier assumptions about the scale of variation of σ_s^2 used in (102)), then it can be shown that for interferometric angles satisfying (110), the decorrelation will be very small [14]. The reflectivity model in (114) is not equivalent to that of a point scatterer. For surface scatterers not satisfying (114), the geometric decorrelation can be reduced using the procedure described in Section 6.3.

6.3. Wavenumber adjustment for an extended scatterer. As suggested in [18], one can use sub-band images (see (79)–(81)) to eliminate the geometric decorrelation described by (108). The imaging kernels in (96) are modified as follows:

$$\begin{aligned} W^{(1)}(l) &\longrightarrow \tilde{W}^{(1)}(l) = e^{-2ik_1l} \tilde{V}(l), \\ W^{(2)}(l) &\longrightarrow \tilde{W}^{(2)}(l) = e^{-2ik_2l} \tilde{V}(l), \end{aligned}$$

where

$$(115) \quad \tilde{V}(l) = \tilde{\tau} \operatorname{sinc}\left(\frac{\tilde{B}l}{c}\right), \quad \tilde{B} = B - |k_2 - k_1|c, \quad \tilde{\tau} = \tau \frac{\tilde{B}}{B},$$

see (79c) and (97). If we assume $\sigma^2(\mathbf{z}) = \sigma_h^2(h)\sigma_s^2(s)$ as in (101), then the new expression for the complex interferogram takes the following form (cf. equation (103)):

$$(116) \quad \begin{aligned} \tilde{Q}(y_u) &= \left\langle \overline{\tilde{\mathcal{I}}^{(1)}(R_y^{(1)})} \tilde{\mathcal{I}}^{(2)}(R_y^{(2)}) \right\rangle \\ &= \frac{\tilde{\tau}^2}{\sin \theta} e^{i\tilde{\Phi}_Q} \sigma_s^2(y_u / \sin \theta) \int \sigma_h^2(h) e^{-2ik \frac{\Delta \theta}{\sin \theta} h} dh \cdot \int \operatorname{sinc}^2\left(\frac{\tilde{B}z'_u}{c}\right) dz'_u, \end{aligned}$$

where, similarly to (85),

$$(117) \quad \tilde{\Phi}_Q = \Phi_Q + \Delta k(2R - x_u^{(1)} - x_u^{(2)}),$$

and Φ_Q is defined in (66). Unlike in (103), the second integral in (116) does not have a complex exponential in the integrand. For the interferometric coherence, we obtain (cf. formula (104)):

$$\tilde{\gamma} = \tilde{\gamma}^{\text{vol}} \tilde{\gamma}^{\text{geom}},$$

where (cf. equations (105) and (106))

$$(118) \quad \tilde{\gamma}^{\text{vol}} = e^{i(\tilde{\Phi}_Q - \Phi_Q)} \gamma^{\text{vol}} \quad \text{and} \quad \tilde{\gamma}^{\text{geom}} = \begin{cases} 1, & |\omega_1 - \omega_2| < \tilde{B}, \\ 0, & \text{otherwise.} \end{cases}$$

With the help of (77), we can see that (118) offers an improvement over (108): $\tilde{\gamma}^{\text{geom}} \geq \gamma^{\text{geom}}$, which means that the noise level in the interferogram has been reduced. For the vertically localized scatterer considered in Section 6.2, this reduces the variance of the elevation computed by (113). When the scatterer is not localized in the vertical direction, increasing the geometric coherence leads to a more accurate estimation of the volumetric term from observations (e.g., to be used in PolInSAR algorithms). Yet along with increasing the coherence, wavenumber adjustment increases the resolution size Δ_R , because $\tilde{B} < B$, see (115) and (50). If we take one sample per resolution element, this can decrease the number of terms in the spatial averaging formula (94) and hence increase the variance of Q^{exper} , see (95). The full analysis of this effect is outside the scope of the current work.

As demonstrated in Section 5.3, wavenumber adjustment removes the dependence of the interferometric phase on the horizontal coordinate, see (89). Comparing the effect of the adjustment on the interferometry of extended scatterers vs. that of point scatterers, we notice that for the former, the complex exponential is removed from the integrand in (106). When condition (79d) is met, this eliminates the decorrelation caused by the presence of multiple scatterers within the main lobe of $V(z'_u)$, see Fig. 5. Of course, it does not mean that one can selectively suppress the returns from some of these scatterers and thus restore the conditions leading to (57). At the same time, for the case of an isolated point scatterer, using (57) in (92) and (93) with no ensemble averaging always yields $|\gamma| = 1$ regardless of condition (79d). Hence, if one chooses to apply the wavenumber adjustment procedure to point scatterers, condition (79d) becomes a deterrent as compared to the more straightforward approach to flat Earth phase removal given by (75). Additional insight into wavenumber adjustment can be gained by considering it in the Fourier domain, as outlined in Appendix A.

7. Conclusions. We have presented a mathematical overview of the cross-track radar interferometry. The use of imaging operators allowed us to identify several issues that often lack attention in the traditional accounts of the area. The most important contributions of the current work are:

- To build the interferogram, one needs to use a modified form of the SAR image given by (56). This form is different from the “output of the matched filter” that is typically considered in the mathematical analysis of SAR imaging, as explained in Section 5.1.
- The absolute phase of the interferogram contains a number of ambiguous terms that cannot be evaluated with the accuracy required for interferometry. Some of these ambiguities are due to insufficient accuracy, e.g., errors in antenna coordinates and misregistration of the original images. Others involve systematic errors, such as those that result from dropping the higher order terms in the far-field approximation (7). At the same time, the difference between the interferometric phases calculated for different points on the image has the level of these ambiguities significantly reduced so that the result appears sufficiently accurate for the purpose of height retrieval.
- The case of isolated point scatterers is the easiest for the analysis of radar imaging and interferometry. Yet it does not fully manifest the significance of wavenumber adjustment (aka spectral range filtering) that is of key importance for radar interferometry of extended scatterers.
- Wavenumber adjustment is a signal processing tool designed for coherence control in the case of extended scatterers. In the Fourier domain (see Appendix A), this procedure can be interpreted as suppressing the returns from the parts of the reflectivity spectrum that do not contribute to both images at the same time.
- The analysis of wavenumber adjustment assumes a δ -correlated extended scatterer. Its conclusions cannot be easily extended to other autocorrelation models, in particular, that of isolated point scatterers.

Additional topics related to radar interferometry that could also benefit from the analysis based on imaging operators include:

- Interferometry of the targets with reflectivity in-between the extremes of a point scatterer and δ -correlated scatterer. One such example is the model

(114); additional examples can be found, e.g., in [20, 17]. These cases may also cover the so-called persistent scatterers, see, e.g., [14, 9, 12, 4].

- Polarimetric target models in the context of reconstruction of the vertical profile of reflectivity known as PolInSAR [8].
- Wavenumber adjustment in the case of reflectivity functions that do not conform to the factorized model (101) (a variable ground slope is considered in [24, 5]).

Appendix A. Wavenumber adjustment in the Fourier domain. Formula (110) establishes a condition for partial coherence of two radar images of an extended scatterer. A common interpretation of this condition involves the analysis of spatial frequencies (see, e.g., [16, Section 4.6]). For a radar operating at the central frequency ω_0 , bandwidth B , and incident angle θ , the spatial frequencies κ^i of the incident pulse observed on the horizontal target plane are

$$(119) \quad \left(\omega_0 - \frac{B}{2}\right) \frac{\sin \theta}{c} \leq \kappa^i \leq \left(\omega_0 + \frac{B}{2}\right) \frac{\sin \theta}{c}.$$

The backscattering is enabled by Bragg resonances (see [19, Chapter 7] and [20, 3, 37, 2]), where for each κ^i from the interval (119) there must be a corresponding spatial frequency $\kappa = -2\kappa^i$ in the spectrum of reflectivity. Hence, the spectral interval of ν involved in the scattering is

$$(120) \quad -2\left(\omega_0 + \frac{B}{2}\right) \frac{\sin \theta}{c} \leq \kappa \leq -2\left(\omega_0 - \frac{B}{2}\right) \frac{\sin \theta}{c}.$$

When the incidence angle changes by $\Delta\theta$, the center of the interval (120) gets shifted by

$$(121) \quad \Delta\kappa = -2\Delta\kappa^i = -2\omega_0 \cos \theta \Delta\theta / c.$$

For the two images to be correlated, the corresponding frequency intervals (120) for $\theta = \theta_1$ and $\theta = \theta_2$ must overlap, where $\Delta\theta = \theta_1 - \theta_2$, see (77). From (119) and (121), it is easy to see that the condition for overlap is given by (110):

$$(122) \quad |\Delta\theta| \leq \frac{B}{\omega_0} \tan \theta.$$

The foregoing argument helps justify the wavenumber adjustment procedure as in (76) and (16). To further corroborate it, we will repeat the analysis of Section 6.3 in the Fourier domain for the case $\sigma_h^2(h) = \sigma_0^2 \delta(h)$, see (107). The locus of all \mathbf{y} and \mathbf{z} will be the line $h = 0$. In addition, the variation of the horizontal coordinate will be restricted to the first Fresnel zone: $|s| \lesssim \sqrt{\lambda R}$. This allows us to use the linearized distances (cf. equations (63)):

$$(123) \quad \begin{aligned} R_{\mathbf{y}_s} &\approx R + y_u - x_u - y_v \frac{x_v}{R} + \frac{(x_v)^2}{2R} \\ &= R - x_u + \frac{(x_v)^2}{2R} + y_s \sin \theta \left(1 - \frac{x_v}{R \tan \theta}\right), \end{aligned}$$

where $(-R + x_u, x_v)$ are the slanted coordinates of an antenna, see Fig. 4. Hereafter, the subscript “ s ” corresponds to the one-dimensional scatterer $h = 0$. In particular, y_s is the horizontal coordinate of the focusing point. Let $\zeta = x_v / (R \tan \theta)$. Using (123), we rewrite the imaging formula (40) as follows:

$$(124) \quad I_s(y_s) = \int W_s(y_s - s) \nu_s(s) ds,$$

where $W_s(s) = W(s \sin \theta(1 - \zeta))$ and $W(\cdot)$ is given by (41). Subsequently, we will use the Fourier representation for $W_s(s)$:

$$(125) \quad W_s(s) = \frac{1}{2\pi} \int \hat{W}_s(\kappa) e^{i\kappa s} d\kappa,$$

where

$$(126) \quad \hat{W}_s(\kappa) = \int W_s(s) e^{-i\kappa s} ds = \pi \frac{c\tau}{B \sin \theta} \chi_{2B \sin \theta/c}(\kappa + 2k \sin \theta(1 - \zeta)),$$

and $\chi_{2B \sin \theta/c}(\cdot)$ is the characteristic function of the interval $[-\frac{B \sin \theta}{c}, \frac{B \sin \theta}{c}]$, see (26). In (126), similarly to (121)–(122), we have neglected the modification of the bandwidth due to the interferometric angle.

We assume that the reflectivity function satisfies

$$(127) \quad \langle \overline{\nu_s(s')} \nu_s(s) \rangle = \sigma_s^2 \delta(s' - s).$$

Expressing the imaging kernels for both antennas via (125) and (126), substituting the results into (124), and using (127), we obtain:

$$(128) \quad \langle \overline{I_s^{(1)}(y_s^{(1)})} I_s^{(2)}(y_s^{(2)}) \rangle = \frac{\sigma_s^2}{2\pi} \left(\pi \frac{c\tau}{B \sin \theta} \right)^2 \int e^{i\kappa(y_s^{(2)} - y_s^{(1)})} \cdot \chi_{2B \sin \theta/c}(\kappa + 2k \sin \theta(1 - \zeta^{(1)})) \chi_{2B \sin \theta/c}(\kappa + 2k \sin \theta(1 - \zeta^{(2)})) d\kappa.$$

When condition (122) is satisfied, the two characteristic functions in the integrand of (128) overlap, and by centering the integration interval, we derive:

$$(129) \quad \langle \overline{I_s^{(1)}(y_s^{(1)})} I_s^{(2)}(y_s^{(2)}) \rangle = \frac{\sigma_s^2}{2\pi} \left(\pi \frac{c\tau}{B \sin \theta} \right)^2 e^{i\kappa_c(y_s^{(2)} - y_s^{(1)})} \frac{2\tilde{B} \sin \theta}{c} \operatorname{sinc} \left(\frac{\tilde{B} \sin \theta (y_s^{(2)} - y_s^{(1)})}{c} \right),$$

where

$$(130) \quad \kappa_c = -2k \sin \theta \left(1 - \frac{\zeta^{(1)} + \zeta^{(2)}}{2} \right)$$

and (cf. (79c))

$$\tilde{B} = \max\{B - k|\zeta^{(1)} - \zeta^{(2)}|, 0\} \equiv \max\{B - |\Delta k|c, 0\}.$$

The phase of the interferogram can be computed from (129) with the help of (56):

$$\begin{aligned} \angle Q(y_s) &= \angle \left(\overline{\mathcal{I}_s^1(y_s^1)} \mathcal{I}_s^2(y_s^2) \right) = 2k(R_{y_s}^{(2)} - R_{y_s}^{(1)}) + \kappa_c(y_s^{(2)} - y_s^{(1)}) \\ &= \Phi_q + (\zeta^{(1)} - \zeta^{(2)})k \sin \theta (y_s^{(1)} + y_s^{(2)}) = \Phi_q + \Phi_{s,\text{fEp}} \left(\frac{y_s^{(1)} + y_s^{(2)}}{2} \right) = \Phi_Q, \end{aligned}$$

where $\Phi_{s,\text{fEp}}(s) = -2\Delta k s \sin \theta$ corresponds to definition (100) given $y_u = y_s \sin \theta$. At the same time, the magnitude of the coherence $|\gamma|$ can be calculated using (128) and the following expressions for the intensities of individual images:

$$(131) \quad \begin{aligned} \langle |I_s^{(1)}(y_s^{(1)})|^2 \rangle &= \frac{\sigma_s^2}{2\pi} \left(\pi \frac{c\tau}{B \sin \theta} \right)^2 \int \chi_{2B \sin \theta/c}(\kappa + 2k \sin \theta_1) d\kappa, \\ \langle |I_s^{(2)}(y_s^{(2)})|^2 \rangle &= \frac{\sigma_s^2}{2\pi} \left(\pi \frac{c\tau}{B \sin \theta} \right)^2 \int \chi_{2B \sin \theta/c}(\kappa + 2k \sin \theta_2) d\kappa. \end{aligned}$$

Formulae (131) imply that

$$(132) \quad \left\langle |I_s^{(1)}(y_s^{(1)})|^2 \right\rangle = \left\langle |I_s^{(2)}(y_s^{(2)})|^2 \right\rangle = \frac{\sigma_s^2}{2\pi} \left(\pi \frac{c\tau}{B \sin \theta} \right)^2 \frac{2B \sin \theta}{c}.$$

According to (128), as the separation between θ_1 and θ_2 increases, the absolute value of the correlation between the two images decreases and ultimately becomes zero. At the same time, the denominator in (93) remains constant. Substituting (129) and (132) into (93) and assuming that co-registration guarantees $B \sin \theta |y_s^{(2)} - y_s^{(1)}|/c \ll 1$, we obtain:

$$(133) \quad |\gamma| = \gamma^{\text{geom}} = \frac{\tilde{B}}{B},$$

which is equivalent to (108) given that $|\Delta\theta| = |\theta_2 - \theta_1| \ll 1$ (see (77)). In other words, whenever $\theta_1 \neq \theta_2$ (which is a necessary condition for interferometry), we have $|\gamma| < 1$.

On the other hand, if we apply the wavenumber adjustment procedure (76)–(79):

$$k_1 = k - \frac{\Delta k}{2}, \quad k_2 = k + \frac{\Delta k}{2},$$

where (see (77))

$$\Delta\theta = \frac{x_v^{(2)} - x_v^{(1)}}{R} \quad \text{and} \quad \Delta k = k \frac{\Delta\theta}{\tan \theta},$$

then the imaging kernels for individual antennas are given by (cf. formula (126))

$$(134) \quad \begin{aligned} \hat{W}_s^{(1)}(\kappa) &= \pi \frac{c\tau}{\tilde{B} \sin \theta} \chi_{2\tilde{B} \sin \theta/c}(\kappa + 2k_1 \sin \theta_1), \\ \hat{W}_s^{(2)}(\kappa) &= \pi \frac{c\tau}{\tilde{B} \sin \theta} \chi_{2\tilde{B} \sin \theta/c}(\kappa + 2k_2 \sin \theta_2). \end{aligned}$$

For $k_1 \sin \theta_1 = k_2 \sin \theta_2$, these kernels coincide³, and the corresponding spectral interval of reflectivity in the case $\Delta\theta > 0$ is given by (cf. formula (120)):

$$(135) \quad -2 \left(\sin \theta \left(k + \frac{B}{2c} \right) - k \cos \theta \frac{x_v^{(2)}}{R} \right) \leq \kappa \leq -2 \left(\sin \theta \left(k - \frac{B}{2c} \right) - k \cos \theta \frac{x_v^{(1)}}{R} \right).$$

Therefore, unlike in (128)–(131), the integrals in the numerator and denominator of (93) are taken over the same interval. As long as the inequality (122) holds, this yields:

$$|\tilde{\gamma}| = \tilde{\gamma}^{\text{geom}} = 1,$$

whereas (133) implies $|\gamma| < 1$. As the center of the interval (135) coincides with κ_c of (130), we have:

$$\angle \left(\overline{\langle I_s^{(1)}(y_s^{(2)}) I_s^{(1)}(y_s^{(2)}) \rangle} \right) = \angle \left(\overline{\langle \tilde{I}_s^{(1)}(y_s^{(2)}) \tilde{I}_s^{(1)}(y_s^{(2)}) \rangle} \right),$$

and using (82), we obtain:

$$\begin{aligned} \angle \tilde{\gamma} &= \angle \tilde{Q}(y_s) = \angle \left(\overline{\langle \tilde{I}_s^1(y_s^1) \tilde{I}_s^2(y_s^2) \rangle} \right) = 2(k_2 R_{y_s}^{(2)} - k_1 R_{y_s}^{(1)}) + \kappa_c (y_s^{(2)} - y_s^{(1)}) \\ &= \Phi_q + \Delta k (2R - x_u^{(1)} - x_u^{(2)}) = \tilde{\Phi}_Q, \end{aligned}$$

which coincides with (117).

³Note that due to misregistration, we may still have $\tilde{I}_s^{(1)}(y_s^{(1)}) \neq \tilde{I}_s^{(2)}(y_s^{(2)})$ and $\tilde{I}_s^{(1)}(y_s^{(1)}) \neq \tilde{I}_s^{(2)}(y_s^{(2)})$.

Considering the integral in (128), one can argue that the wavenumber adjustment (134) filters out (i.e., eliminates) the intervals of κ from each term in the integrand that are outside the support of the other term (cf. equation (131)). This gives rise to the alternative name “range spectral filtering” for the wavenumber adjustment procedure.

On the other hand, the model for an isolated point scatterer (see Sections 3.4 and 5) is deterministic rather than stochastic. Although the spectra of the images $\mathcal{I}^{(1)}(y_s)$ and $\mathcal{I}^{(2)}(y_s)$ due to a point scatterer are different, formula (93) with no ensemble averaging will still yield $|\gamma| = 1$ regardless of $\Delta\theta$ because no integral of the type (128) appears in the calculation of the interferogram. As for the experimental formula (94), the main contribution into each of the sums comes from the sample that is closest to the scatterer. Hence, the resulting value of $|\gamma^{\text{exper}}|$ will be close to 1 as well.

Acknowledgments. This material is based upon work supported by the US Air Force Office of Scientific Research (AFOSR) under awards number FA9550-17-1-0230 and FA9550-21-1-0086.

REFERENCES

- [1] R. Bamler and P. Hartl, [Synthetic aperture radar interferometry](#), *Inverse Problems*, **14** (1998), R1–R54.
- [2] F. G. Bass and I. M. Fuks, *Wave Scattering from Statistically Rough Surfaces*, Translated and Edited by Carol B. Vesecky and John F. Vesecky. International Series in Natural Philosophy, Pergamon Press, Oxford-New York, 1979.
- [3] P. Beckmann and A. Spizzichino, *The Scattering of Electromagnetic Waves from Rough Surfaces*, Pergamon Press, New York, 1963.
- [4] F. Bovenga, D. Derauw, F. M. Rana, C. Barbier, A. Refice, N. Veneziani and R. Vitulli, Multi-chromatic analysis of SAR images for coherent target detection, *Remote Sensing*, **6** (2014), 8822–8843.
- [5] G. Brigot, M. Simard, E. Colin-Koeniguer and A. Boulch, Retrieval of forest vertical structure from PolInSAR data by machine learning using LIDAR-derived features, *Remote Sensing*, **11** (2019), 381.
- [6] M. Cheney, [A mathematical tutorial on synthetic aperture radar](#), *SIAM Rev.*, **43** (2001), 301–312.
- [7] M. Cheney and B. Borden, Fundamentals of radar imaging, *CBMS-NSF Regional Conference Series in Applied Mathematics. SIAM, Philadelphia*, **79** (2009).
- [8] S. Cloude, *Polarisation: Applications in Remote Sensing*, Oxford University Press, 2010.
- [9] M. Crosetto, O. Monserrat, M. Cuevas-González, N. Devanthéry and B. Crippa, Persistent scatterer interferometry: A review, *ISPRS Journal of Photogrammetry and Remote Sensing*, **115** (2016), 78–89.
- [10] I. G. Cumming and F. H. Wong, *Digital Processing of Synthetic Aperture Radar Data. Algorithms and Implementation*, Artech House, Boston, 2005.
- [11] L. J. Cutrona, *Synthetic Aperture Radar*, 2nd edition, M. Skolnik, editor, Radar Handbook, 21, McGraw-Hill, New-York, 1990.
- [12] D. Derauw, A. Orban and C. Barbier, Wide band SAR sub-band splitting and inter-band coherence measurements, *Remote Sensing Letters*, **1** (2010), 133–140.
- [13] M. Eineder, C. Minet, P. Steigenberger, X. Cong and T. Fritz, Imaging geodesy — toward centimeter-level ranging accuracy with TerraSAR-X, *IEEE Transactions on Geoscience and Remote Sensing*, **49** (2011), 661–671.
- [14] A. Ferretti, C. Prati and F. Rocca, Permanent scatterers in SAR interferometry, *IEEE Transactions on Geoscience and Remote Sensing*, **39** (2001), 8–20.
- [15] H. Foroosh, J. B. Zerubia and M. Berthod, Extension of phase correlation to subpixel registration, *IEEE Transactions on Image Processing*, **11** (2002), 188–200.
- [16] G. Franceschetti and R. Lanari, *Synthetic Aperture Radar Processing*, Electronic Engineering Systems Series. CRC Press, Boca Raton, FL, 1999.

- [17] G. Franceschetti and D. Riccio, *Scattering, Natural Surfaces, and Fractals*, Elsevier, 2006.
- [18] F. Gatelli, A. Monti Guamieri, F. Parizzi, P. Pasquali, C. Prati and F. Rocca, The wavenumber shift in SAR interferometry, *IEEE Transactions on Geoscience and Remote Sensing*, **32** (1994), 855–865.
- [19] M. Gilman, E. Smith and S. Tsynkov, *Transionospheric Synthetic Aperture Imaging*, Applied and Numerical Harmonic Analysis. Birkhäuser/Springer, Cham, Switzerland, 2017.
- [20] M. Gilman and S. Tsynkov, [A mathematical model for SAR imaging beyond the first Born approximation](#), *SIAM J. Imaging Sci.*, **8** (2015), 186–225.
- [21] R. M. Goldstein, H. A. Zebker and C. L. Werner, Satellite radar interferometry: Two-dimensional phase unwrapping, *Radio science*, **23** (1988), 713–720.
- [22] J. W. Goodman, Statistical properties of laser speckle patterns, in *Laser Speckle and Related Phenomena*, (1984), 9–75.
- [23] M. Guizar-Sicairos, S. T. Thurman and J. R. Fienup, Efficient subpixel image registration algorithms, *Opt. Lett.*, **33** (2008), 156–158.
- [24] R. F. Hanssen, *Radar Interferometry: Data Interpretation and Error Analysis Remote Sensing and Digital Image Processing*, Kluwer Academic Publishers, New York, 2001.
- [25] E. W. Hoen and H. A. Zebker, Penetration depths inferred from interferometric volume decorrelation observed over the Greenland ice sheet, *IEEE Transactions on Geoscience and Remote Sensing*, **38** (2000), 2571–2583.
- [26] J. A. Jackson, B. D. Rigling and R. L. Moses, Canonical scattering feature models for 3D and bistatic SAR, *IEEE Transactions on Aerospace and Electronic Systems*, **46** (2010), 525–541.
- [27] C. V. Jakowatz, Jr., D. E. Wahl, P. H. Eichel, D. C. Ghiglia and P. A. Thompson, *Spotlight-Mode Synthetic Aperture Radar: A Signal Processing Approach*, Springer, 1996.
- [28] D. Just and R. Bamler, Phase statistics of interferograms with applications to synthetic aperture radar, *Applied Optics*, **33** (1994), 4361–4368.
- [29] J.-S. Lee and E. Pottier, *Polarimetric Radar Imaging from Basics to Applications*, Optical Science and Engineering. CRC Press, Boca Raton, 2009.
- [30] G. D. Martino, A. Iodice, D. Riccio and G. Ruello, Equivalent number of scatterers for SAR speckle modeling, *IEEE Transactions on Geoscience and Remote Sensing*, **52** (2014), 2555–2564.
- [31] D. Massonnet and J.-Claude Souyris, *Imaging with Synthetic Aperture Radar*, Engineering Sciences: Electrical Engineering. EFPL Press. Distributed by CRC Press, Lausanne, Switzerland, 2008.
- [32] A. Moreira, P. Prats-Iraola, M. Younis, G. Krieger, I. Hajnsek and K. P. Papathanassiou, A tutorial on synthetic aperture radar, *IEEE Geoscience and Remote Sensing Magazine*, **1** (2013), 6–43.
- [33] C. Oliver and S. Quegan, *Understanding Synthetic Aperture Radar Images*, Artech House Remote Sensing Library. Artech House, Boston, 1998.
- [34] P. A. Rosen, S. Hensley, I. R. Joughin, F. K. Li, S. N. Madsen, E. Rodriguez and R. M. Goldstein, Synthetic aperture radar interferometry, *Proceedings of the IEEE*, **88** (2000), 333–382.
- [35] H. S. Stone, M. Orchard, E. Chang and S. Martucci, A fast direct Fourier-based algorithm for subpixel registration of images, *IEEE Transactions on Geoscience and Remote Sensing*, **39** (2001), 2235–2243.
- [36] Q. Tian and M. N. Huhns, Algorithms for subpixel registration, *Computer Vision, Graphics, and Image Processing*, **35** (1986), 220–233.
- [37] A. Voronovich, *Wave Scattering from Rough Surfaces*, Springer Series on Wave Phenomena, Springer-Verlag, Berlin, 1999.
- [38] M. Wermuth, A. Hauschild, O. Montenbruck and R. Kahle, TerraSAR-X precise orbit determination with real-time GPS ephemerides, *Advances in Space Research*, **50** (2012), 549–559.
- [39] B. Yazıcı, I. Son and H. Cagri Yanik, [Doppler synthetic aperture radar interferometry: A novel SAR interferometry for height mapping using ultra-narrowband waveforms](#), *Inverse Problems*, **34** (2018), 055003.
- [40] B. Yonel, I. Son and B. Yazici, Exact multistatic interferometric imaging via generalized Wirtinger flow, *IEEE Transactions on Computational Imaging*, **6** (2020), 711–726.
- [41] Y. T. Yoon, M. Eineder, N. Yague-Martinez and O. Montenbruck, TerraSAR-X precise trajectory estimation and quality assessment, *IEEE Transactions on Geoscience and Remote Sensing*, **47** (2009), 1859–1868.

- [42] H. A. Zebker and J. Villasenor, Decorrelation in interferometric radar echoes, *IEEE Transactions on Geoscience and Remote Sensing*, **30** (1992), 950–959.

Received July 2020; revised April 2021. Early access July 2021.

E-mail address: mgilman@ncsu.edu

E-mail address: tsynkov@math.ncsu.edu